JGR Oceans

RESEARCH ARTICLE
10.1029/2019JC015366

Large Decadal Changes in Air-Sea CO_2 Fluxes in the Caribbean Sea

Rik Wanninkhof[1], Joaquin Triñanes[2,3], Geun-Ha Park[4], Dwight Gledhill[5], and Are Olsen[6]

[1]Atlantic Oceanographic and Meteorological Laboratory, NOAA, Miami, FL, USA, [2]Laboratory of Systems, Technological Research Institute, Universidad de Santiago de Compostela, Santiago de Compostela, Spain, [3]Cooperative Institute for Marine and Atmospheric Studies, Rosenstiel School of Marine and Atmospheric Science, University of Miami, Miami, FL, USA, [4]Marine Environmental Research Center, Korea Institute of Ocean Science & Technology, Busan, South Korea, [5]NOAA Ocean Acidification Program, Silver Spring, MD, USA, [6]Geophysical Institute, University of Bergen and Bjerknes Centre for Climate Research, Bergen, Norway

Key Points:
- The Caribbean Sea was a CO_2 sink from 2002 to 2018 with large interannual changes in uptake
- Surface water fugacity of CO_2 remained steady till 2010 and increased rapidly thereafter
- The change in trend around 2010 is modulated by changes in sea surface temperature and ocean mixed layer depth

Correspondence to:
R. Wanninkhof,
rik.wanninkhof@noaa.gov

Citation:
Wanninkhof, R., Triñanes, J., Park, G.-H., Gledhill, D., & Olsen, A. (2019). Large decadal changes in air-sea CO_2 fluxes in the Caribbean Sea. *Journal of Geophysical Research: Oceans*, *124*, 6960–6982. https://doi.org/10.1029/2019JC015366

Received 11 JUN 2019
Accepted 6 SEP 2019
Accepted article online 12 SEP 2019
Published online 21 OCT 2019

©2019. American Geophysical Union. All Rights Reserved.

Abstract Sixteen years of surface water CO_2 data from autonomous systems on cruise ships sailing in the Caribbean Sea and Western North Atlantic show marked changes on interannual timescales. The measured changes in fugacity (≈partial pressure) of CO_2 in surface water, fCO_{2w}, are based on over a million observations. Seasonally the patterns are similar to other oligotrophic subtropical regions with an amplitude of fCO_{2w} of ≈40 μatm with low wintertime values, causing the area to be a sink, and high summertime values making it a source of CO_2 to the atmosphere. On annual scales there was negligible increase of fCO_{2w} from 2002 to 2010 and a rapid increase from 2010 to 2018. Correspondingly, the trend of air-sea CO_2 flux from 2002 to 2010 was strongly negative (increasing uptake or sink) at -0.05 ± 0.01 (mol m^{-2} $year^{-1}$) $year^{-1}$ and positive (decreasing uptake) at 0.02 ± 0.02 (mol m^{-2} $year^{-1}$) $year^{-1}$ from 2010-2018. For the whole period from 2002 to 2018, the fCO_{2w} lagged the atmospheric CO_2 increase by 24 %, causing an increase in CO_2 uptake. The average flux into the ocean for the 16 years is -0.20 ± 0.16 mol m^{-2} $year^{-1}$ with the uncertainty reflecting the standard deviation in annual means. The change in multiannual trend in fCO_{2w} is modulated by several factors, notably changes in sea surface temperature and ocean mixed layer depth that, in turn, affected the physical and biological processes controlling fCO_{2w}.

Plain Language Summary Through a unique collaboration with Royal Caribbean Cruise Lines several cruise ships were outfitted with automated surface water carbon dioxide (CO_2) measurement systems, providing weekly observations in the Caribbean Sea over the past 16 years. From over a million measurements, the increase in surface water CO_2 in response to rising atmospheric levels was accurately monitored. The region is, on average, a carbon dioxide sink with large multiyear differences. For the first 8 years, the surface water levels do not change appreciably causing an increase in difference between the air and sea concentrations. This increased differential drives in increase in the air to sea flux of CO_2. Carbon dioxide levels in surface water in the following 8 years actually increased faster than the atmosphere, thereby decreasing the differential and subsequent flux rate. The cause of changes in trends appears associated with changes in the ocean biogeochemistry, linked to sea surface temperature and mixed layer depth, particularly in the middle part of the record.

1. Introduction

There has been a large increase in measurements of fugacity of carbon dioxide in surface water (fCO_{2w}) over the past two decades after realization that the quality of automated measurements was high enough to quantify global ocean CO_2 uptake (Takahashi et al., 2002). Recommendations to provide sustained systematic fCO_{2w} measurements in the world's oceans to estimate global air-sea fluxes were implemented (Bender et al., 2002). The Caribbean Sea was targeted for observations with passenger cruise ships, providing a unique platform for the unattended systems (Figure 1). Through a federal, industry, academic partnership between NOAA, Royal Caribbean Cruise Lines (RCCL) and the University of Miami, the cruise ship *Explorer of the Seas* (EoS) was outfitted with an automated surface water CO_2 measurement system (Pierrot et al., 2009) providing observations on alternating weekly transects in the Eastern and Western Caribbean. The biweekly occupations of the same locations were optimal to determine regional changes in surface water CO_2 levels in

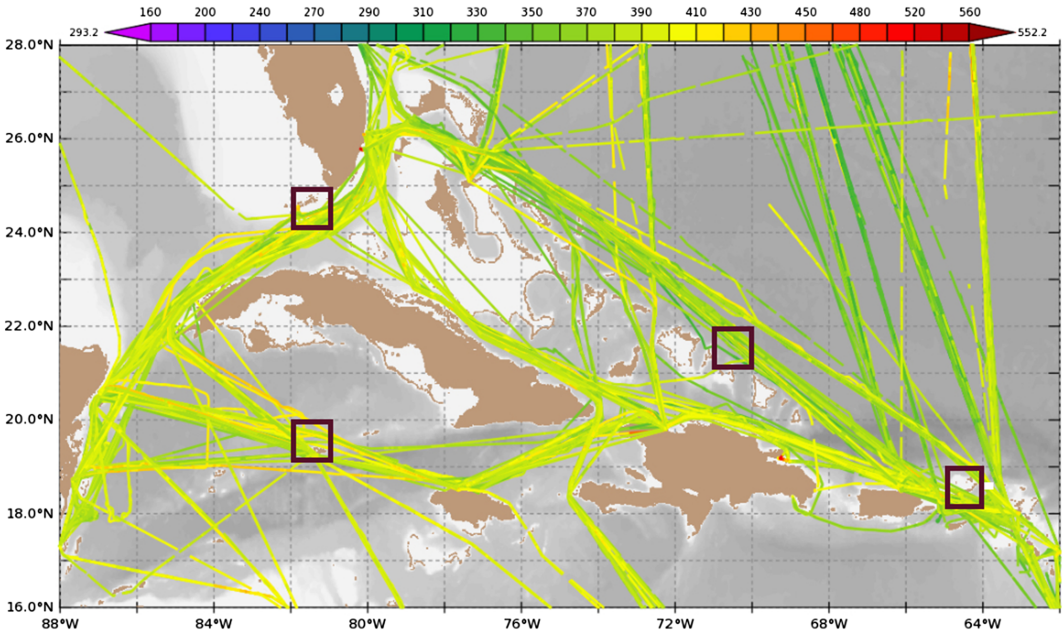


Figure 1. Cruise tracks of the *Explorer of the Seas* (*Eos*), the *Equinox*, and the *Allure of the Seas* in the Caribbean. The squares are the locations where the seasonal patterns for 2017 are discussed in detail (see text and Figure 5). The magnitude of fCO_{2w} is shown with the color bar. The figure was created using the graphical query interface of SOCAT (www.socat.info).

support of ocean acidification and ocean carbon cycle research in an area with significant coral reefs that are vulnerable to changes in temperature and CO_2 levels (Kleypas, 1999).

The cruise ship changed homeport from Miami FL to Port Elizabeth NJ and the routes changed in 2008, foregoing the Western Caribbean occupations and adding cruises to Bermuda. In 2012, the EoS was repositioned to the Pacific and other RCCL ships were outfitted with underway CO_2 systems that covered similar transects as the EoS but on more irregular and seasonal basis. From 2015 onward, two cruise ships, the *Celebrity Equinox* and *Allure of the Seas*, have covered the area.

From 2002 to 2018 a total of 510 voyages with automated fCO_{2w} measurements were completed by the RCCL cruise ships. They cover a region spanning 16–28°N and 88–62°W (Figure 1). This represents the northern Caribbean Sea and the western Atlantic, north of the Caribbean island chain. Over the 16 years, there are at least biweekly occupations at the beginning of the record, from 2002 to 2007, and towards the end, from 2014 to 2018, with gaps in the years in between. The temporal and spatial gaps were filled by regressions with position, remotely sensed sea surface temperature (SST), modeled sea surface salinity (SSS), and modeled mixed layer depth (MLD). This does not unduly impact the quantification of conditions and changes in fCO_{2w} and air-sea CO_2 fluxes over the time period.

The Caribbean Sea is largely oligotrophic with low nutrient concentrations in surface water. However, several local environmental factors can impact its nutrient and carbon dynamics. Episodic riverine influence from the Orinoco River increase biological productivity in the southwestern part of the region, based on observed lower salinity and remotely sensed color (Lopez et al., 2013). Runoff and other coastal influences from the islands have an impact on the local CO_2 dynamics and flux estimates (Melendez Oyola et al., 2018). Hurricanes leave an imprint on fCO_{2w} through large effluxes during the extreme wind events and subsequent decreases in fCO_{2w} caused by lower SST and enhancement of biological productivity due to enhanced nutrient exchange from below the mixed layer (Huang & Imberger, 2010; Wanninkhof et al., 2007). The riverine, island, and hurricane influences are significant at local and short time scales but do not show a large impact on seasonality or the regional scale patterns and multidecadal trends of air-sea CO_2 fluxes for the whole region.

The canonical view that the surface inorganic carbon dynamics in the region are largely driven by temperature and processes impacted by temperature holds largely true. However, like the ocean time series stations

in the oligotrophic gyres, near Hawaii (HOT) and Bermuda (BATS), there are multiyear trends that cause the surface water CO_2 increases to deviate from the expected rate of increase (Bates et al., 2014; Dore et al., 2009). The divergent multiyear trends observed in the Caribbean are significantly greater than observed at BATS and HOT for the time period in the references listed. This is unexpected because the shallow MLD, relatively low productivity, and strong stratification should cause the fCO_{2w} increases to be largely controlled by atmospheric CO_2 increases, leading to fCO_{2w} increases of about 2 μatm/year.

The multiyear changes impact the rate of ocean acidification (OA), which is of concern in the region where coral reef cover has declined by over 50% in the last 5 decades due to multiple human stressors (Jackson et al., 2014). The current observation-based estimates of OA for the region rely on empirical correlations between inorganic carbon chemistry versus SST and SSS from the earlier years of this observation program from which an ocean acidification product suite was developed (Gledhill et al., 2008). In this model, annual increases in atmospheric fCO_2 are directly coupled to surface ocean acidification rates with subannual variability governed primarily by SST. The results of the current effort indicate that this approach can be fine-tuned with the 16-year record of observations showing the multiannual anomalies in trends in fCO_{2w}.

Seasonal changes in fCO_{2w} in the Caribbean were first detailed by Olsen et al. (2004) based on the first year (2002) of cruise data from the EoS. The fCO_{2w} levels were closely related to SST and, thus, had lower values in winter and higher in the summer. This annual cycle of fCO_{2w} is such that in the wintertime the region is a CO_2 sink and during the summer is a CO_2 source. Olsen et al. (2004) created a simple but robust algorithm relating fCO_{2w} to SST and location based on the 2002 data:

$$fCO_{2w} = 10.18\times SST + 0.5249\times Lat - 0.2921\times Lon + 52.19,\ r^2 = 0.87 \quad (1)$$

where SST is in °C; Lat is latitude in fractional degrees (North); and Lon is longitude as negative degrees (East). The root-mean-square (RMS) uncertainty of calculated fCO_{2w} was 5.7 μatm.

Equation (1) reflects the strong relationship of fCO_{2w} with SST. It also indicates that at constant SST, fCO_{2w} will be on average 5 μatm higher in the southern part (15°N) than in the northern part (25°N) and 8 μatm higher in the western part (88°W = −88°E) compared to the eastern boundary of the region (62°W). These spatial gradients are relatively small compared to the ≈40-μatm seasonal amplitude associated with a 4 °C change in SST from winter to summer in the region.

Park and Wanninkhof (2012) analyzed 8 years of fCO_{2w} data from 2002 to 2009, in the northeastern part of the region, north of Puerto Rico, predominantly from the EoS. During this time period the fCO_{2w} increased ≈9 μatm, compared to expectations that it should have changed by ≈18 μatm in response to atmospheric CO_2 increases. The stagnation was attributed primarily to wintertime fCO_{2w} increasing very slowly over this time period. This was caused by anomalously high wintertime SST in 2002–2003 and lower wintertime SST in 2008–2009. Winter MLD also increased toward the end of the time period. As a result, the air-water fugacity of CO_2 difference, ΔfCO_2, became more negative in wintertime causing an increase of the CO_2 sink strength in the region for the 2000–2009 period.

Here we build on the previous work, and extend the time series and analyses from 2002 to the spring of 2018. Data products such as wind speed needed to determine the fluxes along with remotely sensed SST, modeled SSS, Normalized Fluorescence Line Height (NFLH), and modeled MLD are used to interpret to results. The sources of these data are detailed in the data section. Instrumental procedures, time series analyses, mapping procedures, and flux calculations are described in the methods section. The seasonal cycles and multiyear trends of the variables of interest are described, and air-sea CO_2 fluxes over the region are quantified. The marked changes from a stagnant annual average fCO_{2w} over the first part of the record from 2002 to 2010 to a larger than atmospheric rate of increase in fCO_{2w} from 2010 to 2018 are quantified. The causes thereof are discussed and deconvolved into temperature, gas exchange, and a residual attributed to biological and mixing (B&M) components.

2. Data and Data Products

In this paper, three different datasets are used and compared. The following nomenclature is used: observational datasets from the cruise ships using the time and position of measurements are referred to as

observations; these data are binned and averaged on a 1° × 1° space scale and monthly timescale (1° × 1° × mo) and are called gridded data (product). The gridded data are useful to determine biases between observed SST and SSS, and remotely sensed SST and modeled SSS. They are also used to determine if gridding and extrapolation procedures impact the interpretation. For the whole region spanning 16°N–28°N and 88°W–62°W, the fCO_{2w} data are extrapolated using multilinear regressions (MLRs) with position, SST, SSS, and MLD as described below. They are used in conjunction with monthly remotely sensed SST, wind, and NFLH, and modeled SSS on the same grid and are referred to as the (gridded) mapped product. This product is the basis of the trend estimates and the explanation of trends. Using the gridded mapped product, the trends in fCO_{2w} and flux for the whole time period and area can be determined without artifacts caused by data gaps.

The field observations were obtained from the three cruise ships listed above totaling over 1 million data points over the 16-year period from March 2002 to 2018. They are posted on the website: www.aoml.noaa.gov/ocd/ocdweb/occ.html per cruise and ship, along with pertinent metadata. The data are archived in the NCEI Ocean Carbon Data System (www.nodc.noaa.gov/ocads/). Data are also collated annually in the Surface Ocean Carbon ATlas, SOCAT (Bakker et al., 2016) and LDEO (Takahashi et al., 2017) data products. Here we use the original data as served from the AOML website. The fCO_2 data are the same for all sites but the quality control procedures and flags differ slightly. Only data with quality control flag 2 (= good data) are used, which are over 98 % of the observations.

For the determination of the fugacity of CO_2 in air, fCO_{2a} the average monthly atmospheric CO_2 mole fraction (XCO_{2a}) product based on weekly measurements at the stations at Key Biscayne, FL, USA (KEY; 26°N, 80°W), and Ragged Point, Barbados (RPB; 13°N, 59°W) are used. They are obtained from the flask sampling network of the Global Monitoring Division of the Earth System Research Laboratory (GMD/ERSL/NOAA; Dlugokencky et al., 2017). These values are quality controlled at GMD and fit to the annual seasonal cycle (see www.esrl.noaa.gov/gmd/ccgg/mbl/data.php). The monthly product is considered representative for the whole region. The difference in monthly mean between the KEY and RPB products from 2002–2018 is 0.6 ± 0.6 ppm (n = 189) with KEY values being on average higher.

Support data used for analyses are on the same 1° × 1° × mo grid as the mapped fCO_{2w}. Wind speeds are from the updated cross-calibrated multiplatform wind product 2 (Atlas et al., 2011). The 1° × 1° × mo mean neutral wind at 10-m height $<u_{10}>$, and its second moment $<u_{10}^2>$ is determined from the ¼ degree, 6-hourly product from Remote Sensing Systems (www.remss.com). The SST product is the Optimum Interpolated SST, OISST (Reynolds et al., 2007). It uses data from ships, buoys, and satellites to generate the analyzed fields. For the OISST, the reference SST is from buoys, and the SST from ships in this product are adjusted to the buoy data by subtracting 0.14 °C. The OISST is on average 0.25 ± 0.40 °C (n = 8,191) lower than SST measurements from the cruise ships when comparing the 1°-gridded data product for the particular month with OISST product. The SST probes on the cruise ships have accuracies better than 0.01 °C, and while the offset is within the standard deviation, it is assumed the difference is real and attributed to the near-surface cool skin (Soloviev & Schlüssel, 1996).

No MLD determinations were made on the cruises and limited observational estimates from other sources are available. The profiling float program, Argo, produces a global MLD product in near real time (Holte et al., 2017). However, Argo only has limited deployments in the Caribbean and no MLD product is available for the region. The MLDs used here are from a numerical model (HYCOM; https://hycom.org/regional). The MLDs are based on a density contrast of 0.03 between surface and subsurface (de Boyer Montégut et al., 2004).

The SSS data used were also extracted from this model, SSS_{hycom}. The SSS_{hycom} is on average 0.1 ± 0.28 (n = 8,191) greater than the ship-based 1° × 1° × mo data product. The difference does not impact the results or interpretation as the SSS has a weak influence on the fCO_{2w} calculated from the MLRs.

NFLH, which is used as a proxy for biological productivity, was retrieved from the moderate resolution imaging spectrophotometer, MODIS. MODIS flies on the satellites AQUA and TERRA. NFLH is a relative measure of water-leaving radiance associated with chlorophyll fluorescence. The level 3 data used are at 1° × 1° × mo resolution and are obtained from http://oceancolor.gsfc.nasa.gov/cgi/l3 website.

3. Methods

3.1. Instrumentation

The fCO_{2w} levels are measured by infrared (IR) analysis of headspace gas equilibrated with water in an equilibration chamber. The gas in the headspace is partially dried (≈>75%) before measurements. The procedures and instrumentation are based on a community design described in Pierrot et al. (2009). The instruments are manufactured by General Oceanics INC. and have performed to high accuracy specifications. The instruments have shown agreement to within 1 μatm with other state-of-art systems in intercomparison studies (Y. Nojiri *et al*., personal communication, February 2009). The IR sensor (LI-COR 6262) is calibrated every 4.5 hr against four standard gasses supplied by the GMD/ESRL/NOAA, traceable to the WMO CO_2 mole fraction scale. The CO_2 concentrations in the standards span the range of values encountered along the ship tracks. Several different versions of the instrument have been deployed on the ships over the years but overall measurement principles and accuracies, estimated at better than 2 μatm, have remained the same.

Pressure in the headspace and temperature of the water in the equilibrator and near the seawater intake, assumed equivalent to SST, are measured at high accuracy. Equilibrator temperature is obtained with a Hart RS thermistor accurate to ±0.002 °C. The pressure is measured by a Setra model 270 barometer which is accurate to 0.1 mbar (hPa). SST and salinity are determined by a Seabird thermosalinograph accurate to 0.01 °C and 0.01 based on factory specifications. As conductivity values used to calculate salinity change due to fouling, the in situ observations probably are less accurate than specification but the uncertainty in salinity has negligible impact on the calculation of fCO_{2w}.

The water intake for the underway pCO_2 instrument and thermosalinograph is near the bow thruster cavity on the ships at a depth of 1.5 m. The shallow depth of the intake and operation of the bow thruster can cause bubble entrainment near ports and in heavy seas. Data obtained under these conditions are flagged and not used in the analyses. Cruises follow a fixed route with occasional deviations due to weather, such as averting heavy seas during and immediately after hurricanes. Typical cruise speeds are 22 knots that with sampling every 2.5 min, yields a sample approximately every 1.7 km except for 35 min every 4.5 hr when four calibration gases and a CO_2-free reference gas are analyzed followed by four atmospheric CO_2 measurements. This causes a distance of 24 km (≈1/4°) without fCO_{2w} measurements. The air for the atmospheric measurements is obtained from an intake mounted near the bow of the ship and piped to the infrared analyzer. Air measurements do not cover the entire record. They were started on the EoS in 2008 and on the *Equinox* in May 2015. Due to challenges installing the airline that needs to be strung up eight decks and forward in the ship's interior there is no air intake line on the *Allure of the Seas*. As there are extensive periods when no air measurements are available, the values used here were determined from two locations in the MBL CO_2 product as described in the data section.

3.2. Calculation of fCO_2

The calibrated values of XCO_2 from the IR analyzer are accurate to within 0.2 ppm based on the certified values of the calibration gases that are traceable to the WMO scale, and uncertainties in their interpolation. The XCO_2 values are converted to fCO_{2eq} (μatm) values following Pierrot et al. (2009):

$$fCO_{2eq} = XCO_{2eq} \times \left(P_{eq} - pH_2O\right) \times f\left(T_{eq} P_{eq}\right) \quad (2)$$

where eq refers to equilibrator conditions. P_{eq} is the pressure in equilibrator headspace and the pH_2O is the water vapor pressure calculated according to equation (10) in Weiss and Price (1980). The T_{eq} is the temperature of water in the equilibrator. The function f(T,P) is the fugacity correction (Weiss, 1974). The fugacity is the partial pressure of CO_2 corrected for nonideality of the gas. The virial coefficients used in the correction as well as the appropriateness of the correction are under debate. The magnitude of the correction (f(T,P) ≈0.997) for converting from pCO_2 to fCO_2 is about ≈1 μatm at the fCO_2 ranges encountered, so the uncertainties in the correction have no effect on the conclusions. The fCO_{2eq} is corrected to surface water values using the intake temperature (SST) according to the empirical relationship that Takahashi et al. (1993) developed for North Atlantic surface waters:

$$fCO_{2w} = fCO_{2eq} \times e^{(0.0423(SST - Teq))} \quad (3)$$

on average $SST - T_{eq} = 0.12 \pm 0.28$ °C (n = 667,865). The SST is higher than T_{eq} because of the warm SST in

the region and lower air temperatures in the air-conditioned ship, in contrast to most ships where water warms once inside.

The fCO_{2a} (μatm) are calculated from XCO_{2a} according to:

$$fCO_{2a} = XCO_{2a} \times (P - pH_2O) \times f(SST, P) \quad (4)$$

here P is the ambient pressure at sea level, pH_2O is determined at SST, and f (SST, P) is the fugacity correction.

3.3. Calculation of Air-Sea CO_2 Flux

For the determination of the air-sea CO_2 flux, F_{CO2} (mol m^{-2} $year^{-1}$), a bulk formulation is applied to the data from the gridded mapped product:

$$F_{CO2} = k \times s \times \Delta fCO_2 \quad (5)$$

where ΔfCO_2 is ($fCO_{2w} - fCO_{2a}$), s is the seawater CO_2 solubility (Weiss & Price, 1980), and k is the gas transfer velocity parameterized as a function of wind speed (Wanninkhof, 2014):

$$k = 0.251 \times <u_{10}^2> \times (Sc/660)^{-1/2} \quad (6)$$

where $<u_{10}^2>$ is the monthly second moment of the 6-hourly wind speeds reported in cross-calibrated multiplatform wind product 2, accounting for the impact of variability of the wind speed on k. The Sc is the Schmidt number of CO_2 in seawater determined as a function of temperature from Wanninkhof (2014).

3.4. Gridded Mapped fCO_{2w} Product Using Multilinear Regressions

Monthly fCO_{2w} fields for the region were created in the following fashion. Annual MLRs were determined from the fCO_{2w} data that were binned and averaged on a 1° × 1° × mo grid similar to the approach of Olsen et al. (2004). To take advantage of improved regional products of salinity and mixed layer depth these variables were included in the MLRs. For SST both a linear and logarithmic dependence were checked but little difference was observed in the fit, and a linear SST dependence was used. The functional form for the MLR fit is as follows:

$$fCO_{2w,mapped} = a\,Lon + b\,Lat + c\,SST + d\,MLD + e\,SSS + f \quad (7)$$

MLRs were determined for each year, so no assumptions about annual fCO_{2w} trends had to be made. The coefficients and their standard errors for each annual MLR are provided in Table 1. SST and location are the strongest predictors. Multicollinearity was checked for the MLRs created for each year. To determine if two or more of the independent parameters (predictors) were correlated, variance inflation factors (VIFS) were calculated and presented in Table 1. The VIFs were well below 5, considered the threshold for multicollinearity. The exception is for 2008 when the VIF for Latitude was 5.7. The residuals of mapped $fCO_{2w,mapped}$ versus the gridded fCO_{2w} data product (1° × 1° × mo) for pixels with fCO_{2w} observations show no spatial or seasonal patterns.

3.5. Determination of controls of fCO_{2w}

For investigation of processes controlling fCO_{2w}, the monthly changes in fCO_{2w} are decomposed into a temperature term, an air-sea CO_2 flux term, and a residual that is controlled by biological processes and mixing:

$$\delta fCO_{2w}(Total) = \delta fCO_{2w}(SST) + \delta fCO_{2w}(F_{CO2}) + \delta fCO_{2w}(B\&M) \quad (8)$$

where δ is the monthly time derivative such that δfCO_{2w} (Total) is the monthly change in fCO_{2w}. The δfCO_{2w} (SST) is the monthly change in fCO_{2w} due to temperature change:

$$\delta fCO_{2w}(SST) = fCO_{2w}(SST_{i+1}) - fCO_{2w}(SST_{(i)}) \times e^{(0.0423 \ \Delta SST)} \quad (9)$$

This is referred to as the thermodynamic effect, where the subscripts i and i + 1 are the values for consecutive months. δfCO_{2w} (F_{CO2}) is the monthly change in fCO_{2w} due to the air-sea CO_2 flux. This is determined in the

Table 1
Coefficients for the MLR for Each Year[a]

	a	b	c	d	e	f	Error		
	(LON)	(LAT)	(SST)	(MLD)	(SSS)	(Icept)	$fCO_{2w,MLR}$	r^2	#points
2002	**−0.32**	**0.45**	**10.29**	**−0.04**	**0.77**	**24.4**	4.7	0.90	537
	0.04	*0.11*	*0.18*	*0.02*	*0.72*	*25.8*			
	1.5	1.7	1.3	1.1	1.2				
2003	**−0.56**	**0.32**	**9.24**	**−0.09**	**1.11**	**32.6**	5.2	0.86	731
	0.03	*0.09*	*0.17*	*0.02*	*0.66*	*24.6*			
	1.2	1.4	1.3	1.2	1.3	1.2			
2004	**−0.42**	**0.82**	**10.34**	**−0.20**	**2.78**	**−55.4**	5.2	0.92	740
	0.03	*0.09*	*0.17*	*0.01*	*0.63*	*23.6*			
	1.2	1.5	1.8	1.4	1.6	1.2			
2005	**−0.43**	**0.49**	**8.71**	**−0.07**	**7.30**	**−172.0**	6.6	0.85	664
	0.04	*0.12*	*0.18*	*0.02*	*0.85*	*32.1*			
	1.1	1.5	1.6	1.4	1.6	1.1			
2006	**−0.31**	**1.13**	**9.60**	**−0.19**	**2.56**	**−26.6**	5.0	0.89	670
	0.03	*0.08*	*0.16*	*0.02*	*0.70*	*26.1*			
	1.3	1.8	1.5	1.4	1.9	1.3			
2007	**−0.62**	**1.12**	**10.56**	**−0.36**	**2.75**	**−77.8**	7.0	0.79	483
	0.05	*0.15*	*0.32*	*0.03*	*1.33*	*49.0*			
	1.2	2.3	1.8	1.4	2.2	1.2			
2008	**−0.12**	**1.12**	**10.58**	**−0.30**	**3.16**	**−55.8**	5.7	0.95	107
	3.7	5.7	3.0	2.5	1.8	3.7			
	0.43	*0.31*	*0.45*	*0.05*	*1.39*	*59.8*			
2009	**−0.66**	**0.30**	**7.18**	**−0.47**	**0.11**	**131.9**	6.9	0.84	125
	0.22	*0.24*	*0.53*	*0.07*	*1.49*	*58.8*			
	1.5	2.3	2.3	1.8	2.1	1.5			
2010	**−0.53**	**2.02**	**8.48**	**−0.23**	**2.12**	**−10.5**	9.3	0.85	323
	0.17	*0.26*	*0.41*	*0.05*	*1.48*	*51.7*			
	1.5	3.9	3.3	2.8	2.8	1.5			
2011	**−0.32**	**0.98**	**6.65**	**−0.28**	**3.06**	**46.8**	7.2	0.76	305
	0.13	*0.19*	*0.34*	*0.04*	*1.51*	*59.7*			
	1.3	3.0	2.6	1.5	3.1	1.3			
2012	**−0.13**	**1.66**	**10.81**	**−0.33**	**5.56**	**−154.1**	7.3	0.91	358
	0.10	*0.16*	*0.28*	*0.04*	*1.36*	*50.9*			
	1.1	2.4	2.4	1.6	2.3	1.1			
2013	**−0.43**	**1.30**	**11.45**	**−0.47**	**4.45**	**−137.5**	8.2	0.83	219
	0.18	*0.23*	*0.48*	*0.05*	*1.63*	*55.5*			
	1.4	2.6	1.9	1.3	2.0	1.4			
2014	**−0.60**	**0.62**	**9.48**	**−0.18**	**3.26**	**−45.2**	7.0	0.78	362
	0.08	*0.15*	*0.29*	*0.03*	*1.06*	*37.7*			
	1.6	2.3	1.4	1.7	1.8	1.6			
2015	**−0.84**	**0.14**	**7.76**	**−0.18**	**1.20**	**70.0**	6.0	0.82	455
	0.04	*0.11*	*0.27*	*0.02*	*0.90*	*34.5*			
	1.0	2.1	1.6	1.0	1.9	1.0			
2016	**−0.79**	**0.37**	**8.72**	**−0.14**	**4.17**	**−62.7**	6.7	0.82	1001
	0.03	*0.08*	*0.20*	*0.01*	*0.45*	*17.1*			
	1.1	1.3	1.5	1.4	1.2	1.1			
2017	***−0.42***	***0.56***	***9.49***	***−0.22***	***5.65***	***−112.6***	6.2	0.87	974
	0.03	*0.08*	*0.15*	*0.02*	*0.58*	*17.1*			
	2.2	3.2	3.5	1.5	2.1	2.2			

Note. The first row (in bold) gives the coefficients for each variable in the MLR. The second row (in italics) for each annual entry is the error of the coefficient. The third row gives the variance inflation factor.
[a]These regressions are used to create the mapped fCO_{2w} fields for each year using the 1° × 1° × mo gridded data product. $fCO_{2w,mapped}$ = a Longitude + b Latitude + c SST + d MLD + e SSS + f

following manner. First the change in total dissolved inorganic carbon, DIC in the mixed layer is calculated as F_{CO2}/MLD. The DIC change is converted to fCO_{2w} change by combining it with the total alkalinity (TAlk) estimated according to Cai et al. (2010): TAlk = 57.3 × SSS + 296.4. Using $fCO_{2w(i)}$, $TAlk_{(i)}$, $SST_{(i)}$, and $SSS_{(i)}$ as input functions in the CO2SYS program (V2.2, Pierrot et al., 2006), the $DIC_{(i)}$ is

calculated. Then $DIC_{(i+1)} = DIC_{(i)} + F_{CO2}/MLD$. Accordingly, $fCO_{2w(i+1)}$ is calculated with CO2SYS using $DIC_{(i+1)}$, $TAlk_{(i+1)}$, $SST_{(i+1)}$, and $SSS_{(i+1)}$. The change in fCO_{2w} due to F_{CO2} is as follows:

$$\partial fCO_{2w}(F_{CO2}) = fCO_{2w(i+1)} - fCO_{2w(i)} \quad (10)$$

The δfCO_{2w}(B&M) is determined as the residual:

$$\delta fCO_{2w}(B\&M) = \delta fCO_{2w}(Total) - \delta fCO_{2w}(SST) - \delta fCO_{2w}(F_{CO2}) \quad (11)$$

The δfCO_{2w}(B&M) is the monthly change caused by other processes that impact fCO_{2w}, including biological drawdown due to biological production, and remineralization and respiration in the mixed layer, the sum which is referred to as net community production. The term also includes effects of mixing and entrainment of waters with different DIC concentrations (and fCO_{2w}) from below the mixed layer and from lateral transport. The δfCO_{2w} (B&M) also implicitly contains processes that change alkalinity in the mixed layer. Alkalinity increases will lower the fCO_{2w}. While some of the alkalinity effects could, in principle, be determined from changes in salinity due to the strong relationship between salinity and alkalinity, month to month salinity changes are small such that the alkalinity effects on fCO_{2w} are not studied separately but rather included in this residual term.

The fCO_{2w} is not a state variable and the deconvolution described in (8) is not strictly additive. For instance, the δfCO_{2w}(SST) does not change the state variable DIC, while the $\delta fCO_{2w}(F_{CO2})$ and δfCO_{2w}(B&M) terms do impact DIC. However, on monthly basis where the changes are relatively small, a linear approximation as used here is justified. More formal deconvolutions to tease out the processes influencing fCO_{2w} have been performed (Metzl et al., 2010; Takahashi et al., 1993; Thomas et al., 2008) using the state variables DIC and TAlk, and the derivatives of fCO_{2w} with DIC, TAlk, temperature, and salinity. In our case where DIC and TAlk were not measured but rather estimated using salinity and fCO_{2w}, the uncertainty in the estimated of DIC and TAlk changes, along with use of a modeled mixed layer, warrant the simpler approach of using a residual B&M term that includes several processes.

The uncertainties in the deconvolution cannot be easily quantified. They include uncertainty in the flux of ≈20%–30% (Wanninkhof, 2014), uncertainty in MLD estimate, spatial and temporal variability in the grid cell, and nonlinearity of processes changing fCO_{2w}. Therefore, no uncertainty estimate is provided due to challenges in properly determining and propagating the errors in each term. Biases in δfCO_{2w}(Total), δfCO_{2w}(SST), and $\delta fCO_{2w}(F_{CO2})$ will be reflected in the δfCO_{2w}(B&M) term. Accordingly, this is interpreted with caution.

3.6. Deseasonalization Using Harmonic Fits

The seasonal cycle is the primary mode of variability in the region and it exhibits a regular pattern. The fCO_{2w} and SST can be well represented with a harmonic fit. In turn, this fit can be subtracted from the monthly values to more clearly discern the multiannual trends. The seasonal cycles of fCO_{2w} and SST of the gridded data product (1° × 1° × mo) are fit to a harmonic function as detailed in Gruber et al. (1998) and Park and Wanninkhof (2012). For fCO_{2w},

$$fCO_{2w,fit} = fCO_{2w,mean} + a \sin(2\pi\, mo/12) + b \cos(2\pi\, mo/12) \quad (12)$$

where $fCO_{2w,mean}$ is the average of all the fCO_{2w} values for all grid points over the 16-year period (373.6 μatm), mo is the month (1–12), and a and b are fitting parameters optimized through a cost function. Using a = −20.4 and b = −10.6 results in an average root-mean-square error, RMSE between the data and the fit of 1.3 μatm. The same procedure is used for SST, with an average SST of 26.95 °C and a RMSE of 0.005 °C. The monthly average values of fCO_{2w} and SST determined with harmonic fits covering the 16-year period are subtracted from the monthly fCO_{2w} and SST values for the region to obtain a seasonality detrended, or deseasonalized, product. Using the deseasonalized residuals of fCO_{2w} and SST improve the detection of longer-term trends and increases the confidence level of the trends. The detrending procedures do not bias the results and the same multiannual patterns are discerned with the original nondeseasonalized observations and mapped products.

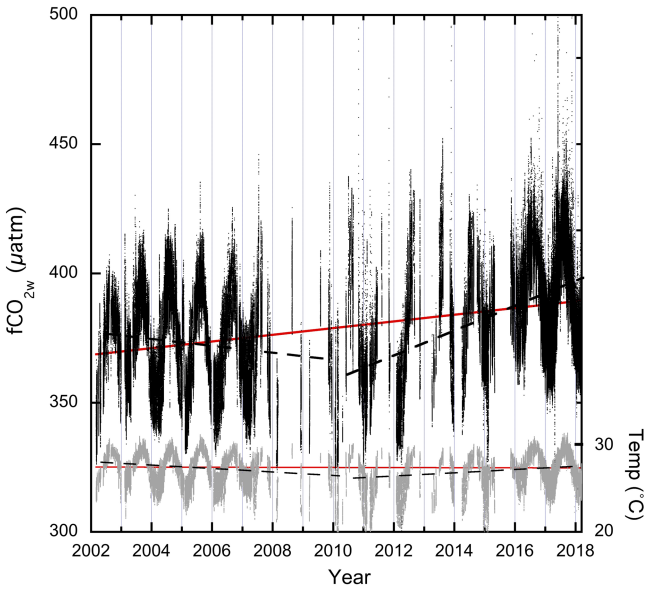


Figure 2. The fCO_{2w} (black points, left axis) and SST (gray points, right axis) show all observations from 2002 to 2018. The solid red lines are the least squares linear fit through all the fCO_{2w} and SST data from 2002 to 2018. The black dashed lines are the fits from 2002 to 2010 and 2010 to 2018. For fCO_{2w} the slopes are 1.30 ± 0.003; −1.37 ± 0.017; and 3.69 ± 0.011 µatm/year, respectively. For SST the slopes are −0.0080 ± 0.0003, −0.178 ± 0.002, and 0.1941 ± 0.001 °C/year, respectively.

4. Results and Discussion

The fCO_{2w} levels are influenced by processes operating over a range of temporal and spatial scales, from hours to decades, and from local to regional. The patterns of fCO_{2w} and air-sea CO_2 fluxes in time and space are discussed for the study region shown in Figure 1 nominally covering 16° N–28°N and 88°W–62°W. Unless noted, the mapped product is used which is on a (1° × 1° × mo) grid from the annually derived MLRs (Table 1).

The lack of observations in the Southeastern Gulf of Mexico north of 25°N can cause the interpolation with MLRs to yield erroneous results in this area as it is affected by other influences than typical for the Caribbean Sea. For example, shelf specific processes on the West Florida shelf, and Mississippi outflow can impact the fCO_{2w} in the Southeastern Gulf of Mexico (Robbins et al., 2018; Xue et al., 2016; Yang et al., 2015). The area is included in the calculation of the total air-sea CO_2 flux, but the results might not be fully representative.

The complete observational dataset of fCO_{2w} and SST from March 2002 to 2018 are plotted against time in Figure 2. The power spectrum of fCO_{2w} shows a singular strong peak at annual time scales. This corresponds with the power spectrum of temperature. This differs from the analysis of mooring based CO_2 data near Bermuda by Bates et al. (2001) that showed a strong daily peak and a broad peak centered on a week based on analysis of monthly data. In both the Bermuda case and this study, the fCO_{2w} and SST spectra match closely, reflecting the role of SST as a direct and indirect driver of fCO_{2w}. The lack of a peak in SST and fCO_{2w} on daily scale for the Caribbean data set is attributed to the signal not being resolved at regional scale of analyses and the ships covering the region at a set schedule. That is, the cruise ships cover the same locations at the same time of day for each cruise itinerary, and the ships spend more time at sea during nighttime such that the diurnal SST and fCO_{2w} cycles at are not well resolved.

4.1. Spatial Differences

Spatial differences are small compared to seasonal changes but they are observable. This can also be inferred from the MLRs of fCO_{2w} (Table 1) that show strong dependencies with position. Based on the MLRs, the average fCO_{2w} values decrease towards the north and toward the east. As temperature is the strongest predictor in the MLRs and there is a correlation between location and temperature, the spatial trends are primarily related to SST. Maps of fCO_{2w}, SST, and SSS are shown in Figures 3a–3f using February and August 2017 as representative examples. The largest spatial differences in fCO_{2w} are apparent in the wintertime (Figure 3a) with high values in the southwest and lower values to the northeast. In summertime (Figure 3b), the highest fCO_{2w} values are in the northwestern part of the region. The relationship of fCO_{2w} with SST is apparent in the patterns. The SSS shows spatial and seasonal variations (Figures 3e and 3f), but the correspondence with fCO_{2w} is not clearly observed, except in the southeastern part of the region where lower SSS waters typically also have lower fCO_{2w} in February (Figures 3a and 3e).

The differences in the annual cycle for four representative locations shown in Figure 1 are highlighted in Figure 4 where the gridded fCO_{2w}, SST, SSS, and MLD products are plotted versus month in 2017. Monthly mean gridded data products from the Florida Current, South of the Florida Keys (pixel centered at 24.5°N, 81.5°W); the Outer Bahamas Banks (Turks and Caicos, 21.5°N, 70.5°W); the Lesser Antilles (18.5°N, 64.5°W); and the western Caribbean (Cayman Islands, 19.5°N, 81.5°W) are shown. The spatial differences in fCO_{2w} and SST are smaller than the extremes in the seasonal cycle (Figures 4a and 4b). Local anomalies are apparent, particularly in SSS (Figure 4c) where a strong minimum is observed in the Lesser Antilles region in the summer and fall, attributed to a combination of Orinoco river outflow and regional precipitation anomalies (Ibánhez et al., 2017). Annual SSS anomalies are seen in other locations as well, such as the minimum observed in summer at the Florida current location. The fCO_{2w} can be directly affected by

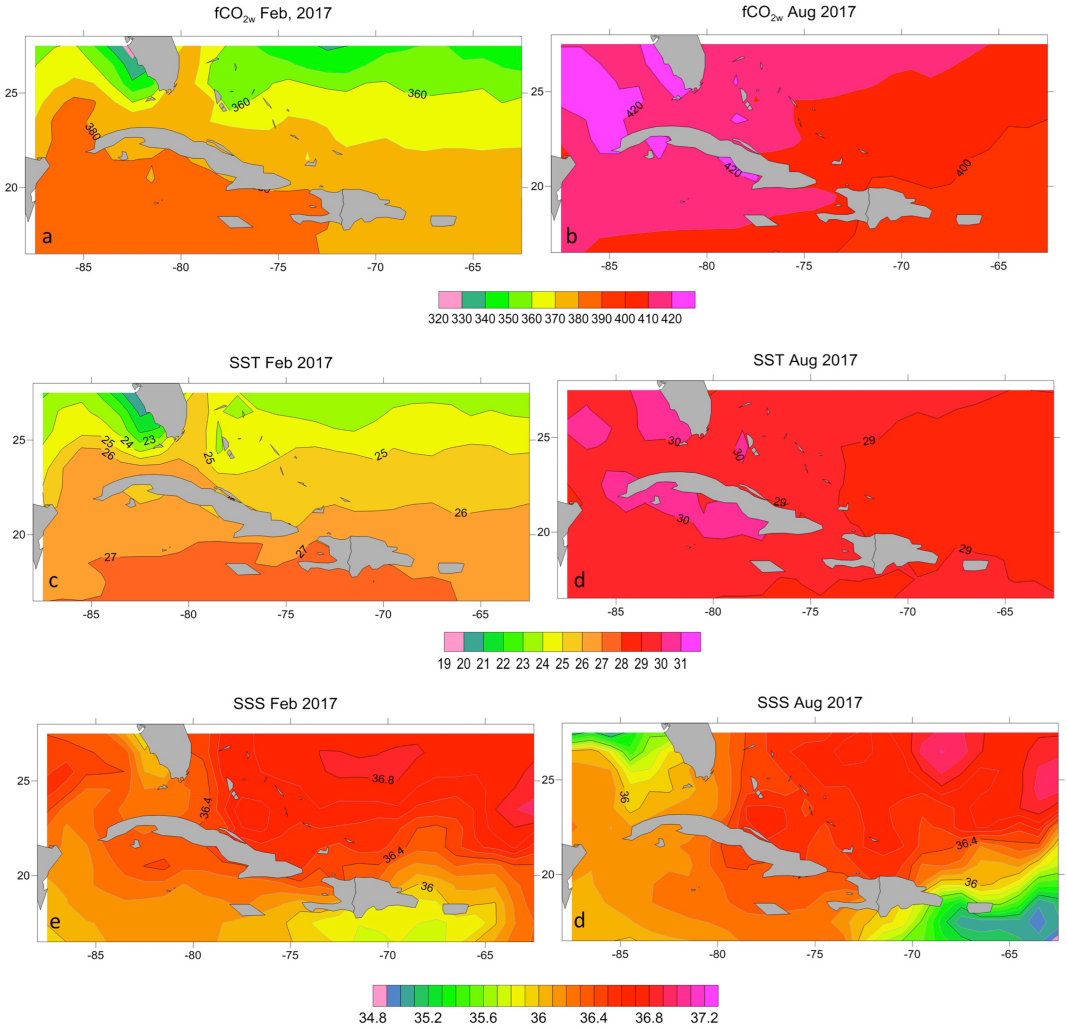


Figure 3. Contour plots of surface water properties in February (left panels) and August (right panels) 2017: fCO_{2w} (a, b); SST (c, d); and SSS (e, f). Color bars with ranges are at the bottom of each panel.

dilution with rainfall (Turk et al., 2010) or, in case of riverine runoff, indirectly as well though enhanced biological productivity from excess nutrients or alkalinity carried by rivers. The low fCO_{2w} levels near the Lesser Antilles appear largely caused by dilution as the observed decrease in fCO_{2w} corresponds to the thermodynamic effect that is 17.5 μatm per unit salinity change (Takahashi et al., 1993). For the low salinities in the Florida current, there is no corresponding reduction in fCO_{2w}, likely because of the increasing SST. The model derived MLD for four locations are given in Figure 4d. All show a seasonal cycle with late summer MLD minima. The Florida current site shows MLD as shallow as 15 m during the summer. The monthly MLD product shows significantly deeper MLD in the western Caribbean compared to the other locations throughout much of 2017.

Local deviations from basin-wide patterns are apparent for other years as well. For example, a maximum in fCO_{2w} of 445 μatm that was observed in the Florida current in July 2016 (not shown) was ≈20 μatm higher than values observed in the adjacent months of 2016 and the fCO_{2w} values observed in July 2017 (Figure 4a). The corresponding SST in July 2016, of 30.3 °C, is only ≈0.4 °C higher than July 2017. Thus, the fCO_{2w} anomaly in July 2016 is about twofold larger than expected from a thermodynamic temperature effect of 4.23% $°C^{-1}$. This high fCO_{2w} value is attributed to entrainment of West Florida Shelf water and is an example of local anomalies that are present throughout the record. However, while local monthly anomalies in SST, SSS, and fCO_{2w} are apparent for different locations, and for different years, the

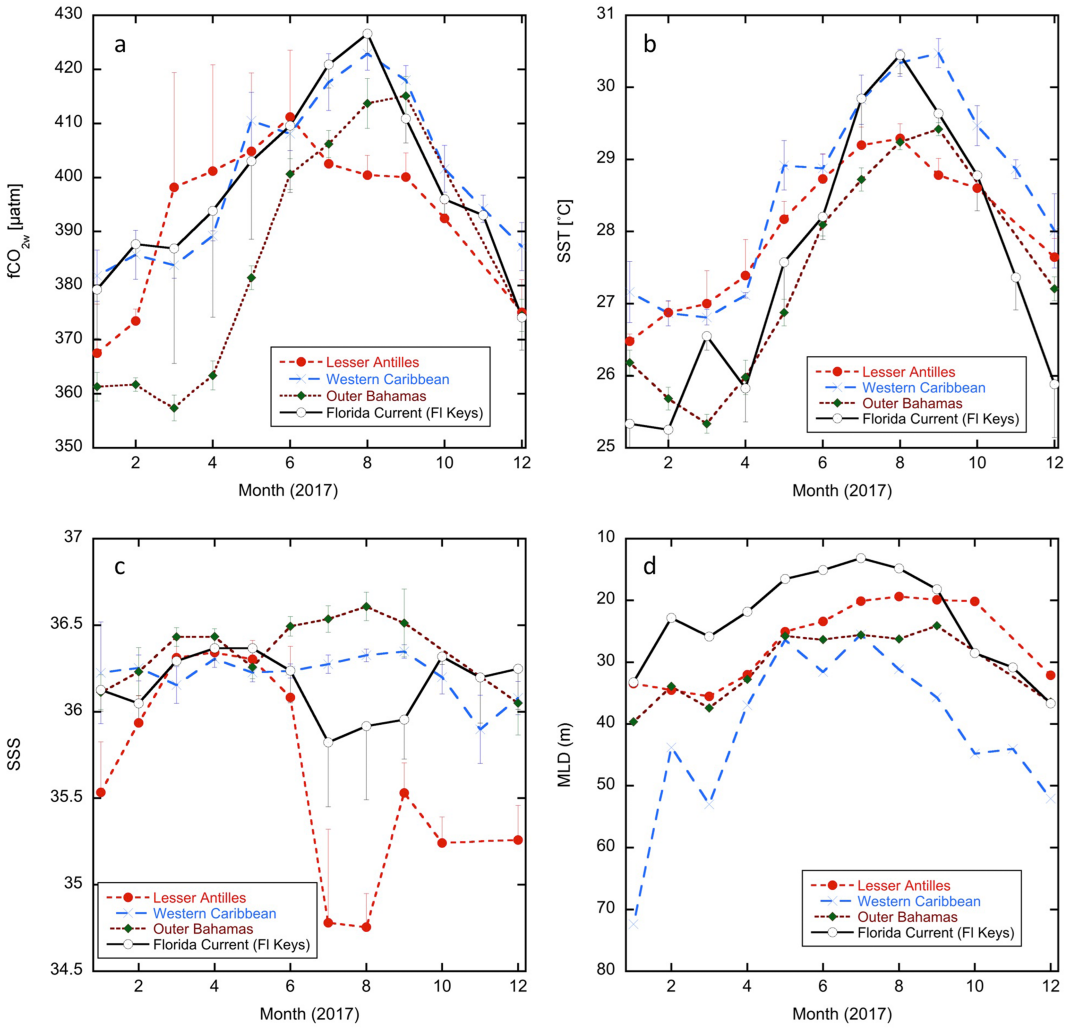


Figure 4. Monthly averaged surface water properties at four locations in the Caribbean based on the gridded data product (1° × 1° × mo) in 2017: Lesser Antilles (18.5°N, 64.5°W) red circles, medium-dashed line; western Caribbean (19.5°N, 81.5°W), blue plusses, long-dashed line; outer Bahamas Bank (21.5°N, 70.5°W), brown diamonds, short-dashed line; and Florida Current (24.5°N, 81.5°W), black open circles, solid black line. fCO_{2w} (a); SST (b); SSS (c); and MLD from the HYCOM model output (d). The vertical lines give the sd of the observations for the particular month in 2017 for the 1° × 1° pixel. For clarity only half the line depicting sd are shown for some points.

region as a whole behaves similarly and, as elaborated upon below, can be viewed as a single entity to assess seasonal to interannual variability and trends.

4.2. Subannual (Seasonal) Patterns

Different factors influence the seasonal fCO_{2w} cycle but seasonal changes in SST are the dominant influence on fCO_{2w}. The thermodynamic dependence of fCO_{2w} to SST is 0.0423 $°C^{-1}$ (4.23% per degree centigrade) due to decreasing solubility and shifting of carbonate equilibrium constants favoring fCO_{2w} increase. The SST changes by ≈4 °C over the annual cycle in the Caribbean and thus has the potential to change fCO_{2w} by ≈60 µatm.

Seasonal changes in MLD can affect fCO_{2w} in differing and opposing ways. Deepening mixed layers can entrain colder water that will thermodynamically decrease the fCO_{2w}. However, the waters can contain higher DIC, which will increase fCO_{2w}. Entrainment and mixing can also supply nutrients, and the resulting primary production can decrease fCO_{2w}. Variability of fCO_{2w} due to mixed layer dynamics and nutrient supply are not well understood (Fawcett et al., 2014). The gradients in inorganic carbon and nutrients below the mixed layer up to the maximum wintertime MLD are small based on GO-SHIP line A22 cruise data (cchdo.

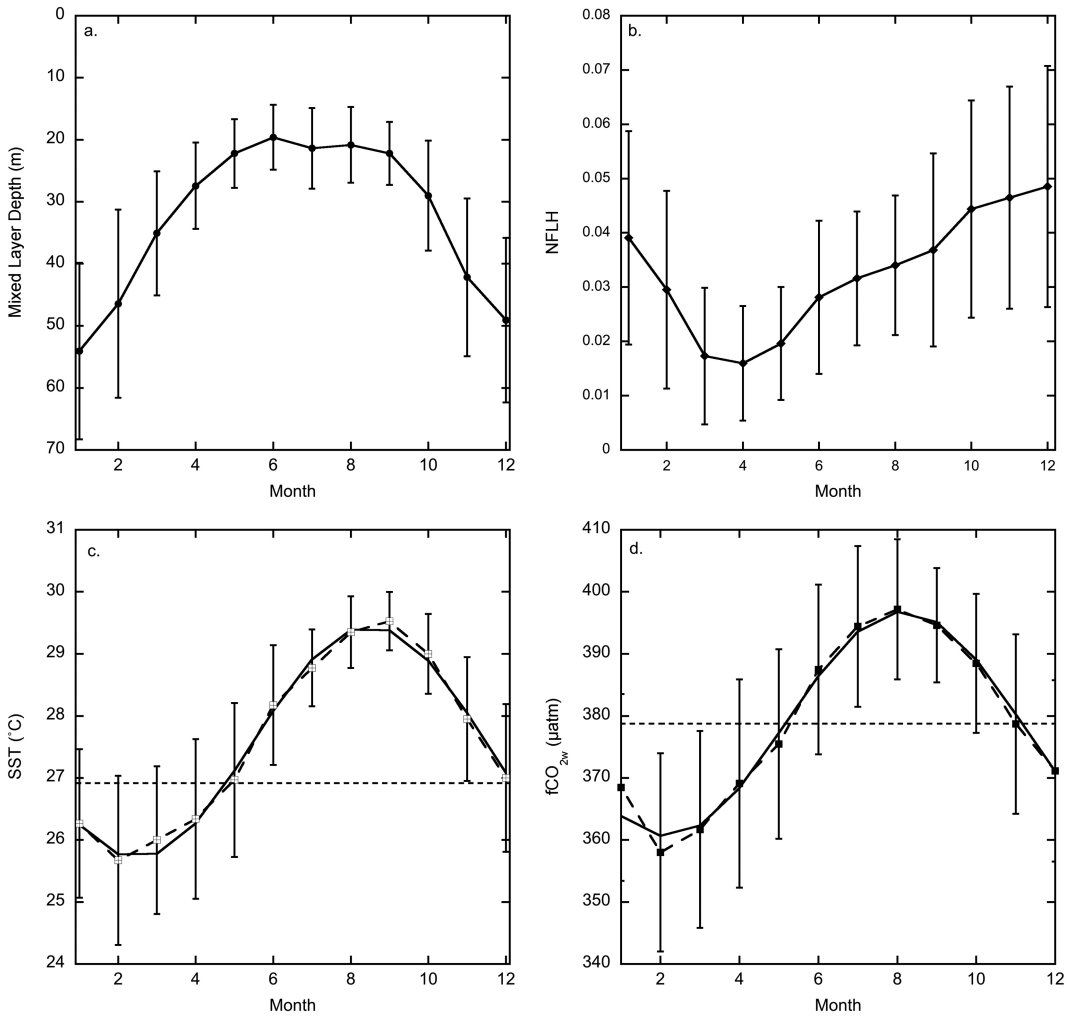


Figure 5. The 16-year monthly averages of the mapped products in the Caribbean with error bars showing the sd of the monthly values. (a) Mixed layer depths from the HYCOM model; (b) Normalized Fluorescent Line Height from MODIS; (c) SST (dashed line) with harmonic fit (thick line); and (d) monthly fCO_{2w} (dashed line) with harmonic fit (thick line). The horizontal dashed line in c and d are the 16-year averages of SST and fCO_{2w}.

uscd.edu) in the eastern part of the region such that entrainment of DIC and nutrients is thought to have a small effect. Lowering of temperature and longer response time to gas transfer are the dominant responses to MLD deepening (Park & Wanninkhof, 2012).

The average seasonal cycle for MLD, NFLH, SST, and fCO_{2w} based on the monthly mapped products for the entire region are shown in Figure 5 with the sd of the monthly values over the 16 years depicted as error bars. Multiannual trends have not been subtracted. The MLD (Figure 5a) shows shallow depths of 21 ± 6 m from May to September and rapid deepening thereafter reaching a maximum average depth of 54 ± 14 m in January after which a shallowing occurs in early spring. The NFLH (Figure 5b) shows a minimum from March to May. The decrease corresponds roughly with the mixed layer shallowing and possibly caused by limited diffusion of nutrients from below during this time.

The seasonal signal in SST (Figure 5c) and fCO_{2w} (Figure 5d) can be well represented using a harmonic function (equation (12)). The seasonal range in fCO_{2w} is 40 µatm and 4 °C in SST with minimum values in February and maximum values in August/September. There is no distinct annual cycle in salinity (not shown).

The close correspondence in phase and shape of the seasonal cycle of SST and fCO_{2w} indicates a strong correlation between them. Figure 6 shows the monthly averaged fCO_{2w} plotted against SST following Lefèvre

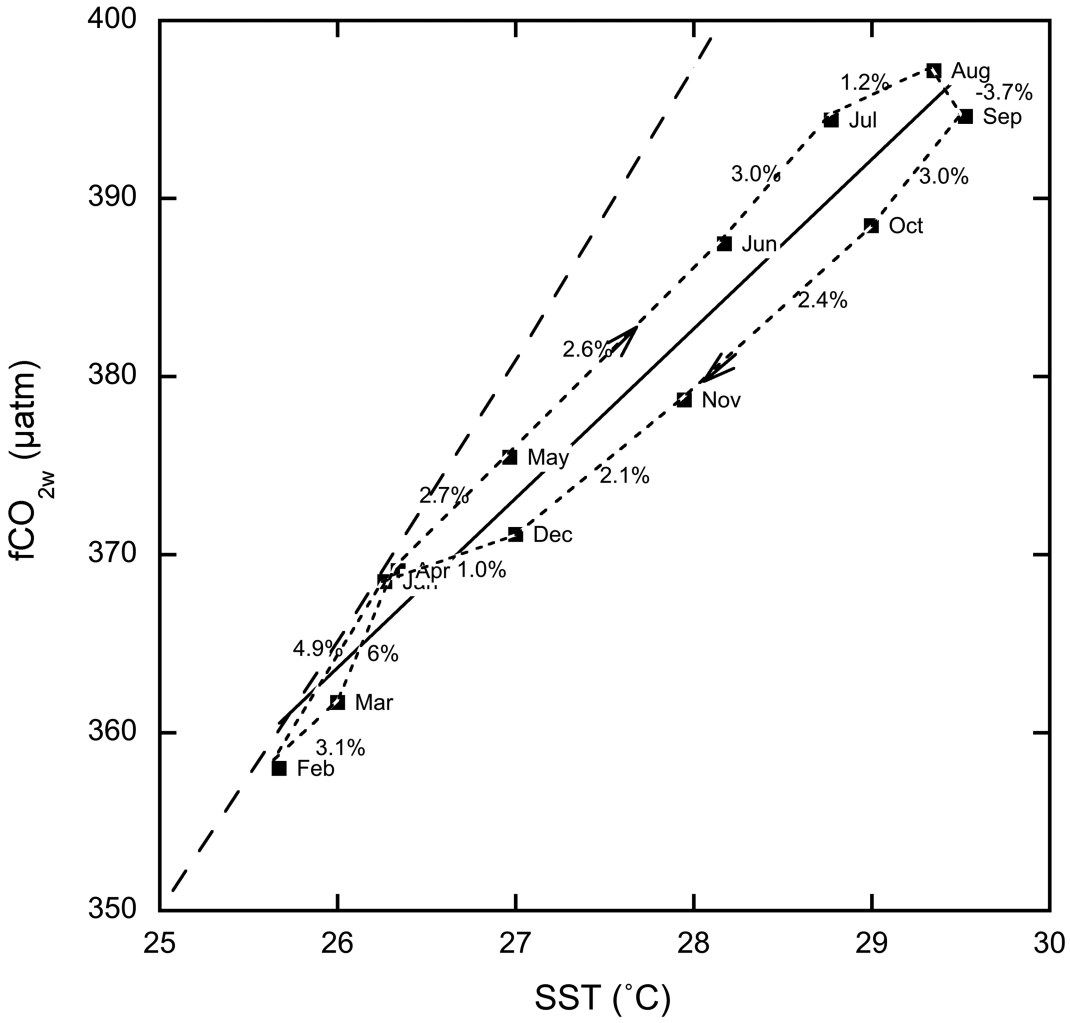


Figure 6. Monthly average fCO_{2w} versus monthly average SST (solid squares) for the gridded product. The thick solid line is the linear fit. The thick dashed line is the thermodynamic dependency (4.23% $°C^{-1}$). The thin dashed line connects the adjacent months and value indicates the percentage change in fCO_{2w} with SST (% $°C^{-1}$) between months.

and Taylor (2002). This diagram illustrates the factors influencing the seasonal cycle in fCO_{2w}. The average change in fCO_{2w} with respect to temperature based on a linear regression of monthly fCO_{2w} versus SST is 9.5 µatm $°C^{-1}$ (2.5% $°C^{-1}$). This is about 60% of the thermodynamic trend, which is shown as a dashed line in Figure 6 indicating that there are counteracting factors impacting the seasonal cycle of fCO_{2w}.

The progression of SST and fCO_{2w} through the year can be delineated by periods of warming from March to August, cooling from September to February, and transitions in February–March, and August–September, respectively (Figure 5c). The seasonal trends in fCO_{2w} are caused by interplay of temperature changes, gas transfer, mixing, and biologically mediated processes. The partitioning of the processes (equation (8)) for the seasonal cycle using gridded product are shown in Figure 7. The deconvolution of fCO_{2w} for the full 16-year record is presented in the attribution section below.

As depicted in Figures 6 and 7, during periods of warming (March–September) the fCO_{2w} increases by ≈8–10 µatm/mo or 2.5%–3.1% $°C^{-1}$. The thermodynamic effect, which is predominant in the annual cycle, increases fCO_{2w}. The net effect of B&M is a drawdown of fCO_{2w} during this warming period. The effect of air-sea gas exchange is of the same magnitude as the B&M impacts (≈1 to 3 µatm/mo) but changes sign during the warming period as it depends on the sign of the ΔfCO_2 gradient. It contributes to increasing fCO_{2w} when the area is a net sink from March to May and to decreasing fCO_{2w} from June to September.

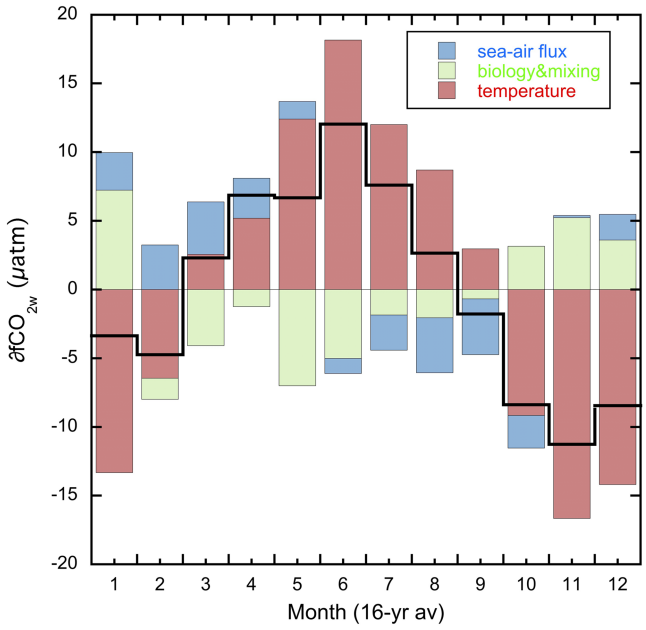


Figure 7. The 16-year average monthly change in fCO_2, ∂fCO_{2w} (solid black line), deconvolved into temperature, δfCO_{2w}(SST), (red), gas exchange, $\delta fCO_{2w}(F_{CO2})$, (blue), and biology and mixing (B&M) components, δfCO_{2w} (B&M; green). The change is that from the preceding month. For example, the change in April (4) is the difference between March and April.

During the cooling period from September to February, fCO_{2w} decreases by ≈8–10 μatm/mo, 2.5%–3% $°C^{-1}$. Again, the thermodynamic effect dominates, with counteracting effects of B&M. The effect of air-sea fluxes reverses from a CO_2 sink in October to a small CO_2 source for the remainder of the cooling period. The B&M effect increases fCO_{2w} during the cooling period except in February. In the transition month from cooling to warming (February–March), the flux into the ocean and B&M are of equal but opposite magnitude. In September, when the transition from warming to cooling occurs, gas evasion counteracts the small net warming with a small contribution of B&M.

The B&M term is calculated as a residual (equation (11)) between the observed monthly fCO_{2w} change, the thermodynamic effect, and the effect of gas transfer. The observed monthly change in fCO_{2w} and the thermodynamic effect are well constrained but biases in the gas flux can be significant at 20%–30%. Generally, the air-sea CO_2 flux term is a smaller contributor. The δfCO_{2w}(B&M) is negative from February to August and positive from September to January. This does not match the NFLH annual progression that shows a minimum in spring and a maximum in December (Figure 5b). However, δfCO_{2w} (B&M) does show broad correspondence with MLD (Figure 5a). This suggests that during periods of shallow mixed layers the biological production is lower but still draws down the fCO_{2w} while during times of mixed layer deepening nutrients are entrained, enhancing productivity and elevating the NFLH. However, due to the deeper MLD the effect on fCO_{2w} is smaller. Also, with deeper MLD remineralized carbon in the form of DIC are brought to the surface that causes the B&M effect to increase fCO_{2w}.

4.3. Temporal Trend

There are clear trends and patterns on multiannual scales in the region. The fCO_{2w} observations versus time show a well-defined seasonal cycle and long-term trends (Figure 2). For the entire observational record from March 2002 to February 2018, the increase in fCO_{2w} is 1.30 ± 0.003 μatm/year but there is a large change in the middle part of the 16-year record, such that it can represented as two linear segments (Figure 2). From March 2002 to February 2010, the observed fCO_{2w} decreases by −1.37 ± 0.017 μatm/year with a reversal in trend to 3.69 ± 0.011 μatm/year from March 2010 to February 2018. The uncertainties are the standard errors in the slope and are small due to the large number of data points. As data coverage is sparser from 2007 to 2011 than at the beginning and end of record, the exact year of turnaround in trend is not well defined in the observations.

A similar trend in the mapped product for the whole region is seen using the deseasonalized monthly residuals, albeit with lower, and only positive trends (Figure 8a). It shows an increase of 1.66 ± 0.09 μatm/year for the entire record. The trend is 0.60 ± 0.21 μatm/year from 2002 to 2010 and 2.55 ± 0.28 μatm/year from 2010 to 2018. While the trends for the observations and mapped values differ, the pattern of little change or deceases in fCO_{2w} for the first 8 years followed by a strong positive trend is the same. The differences between the observations and the gridded mapped product are attributed to a combination of stronger trends in fCO_{2w} and SST in the central region along the tracks where the observations are taken and the use of MLRs in the mapped product that causes features to be smoothed.

To determine the timeframe when the trend changes, 3-year increments are compared, using the mapped product (Table 2). This follows the approach of Fay and McKinley (2013) and allows trends for different increments and lengths to be compared. There is a broad minimum in fCO_{2w} trends centered on the 2008–2011 time frame that cannot be attributed to a single anomalous year. The residuals of the detrended/-deseasonalized fCO_{2w} data (Figure 8a) show large positive and negative anomalies with similar anomalies in SST (Figure 8b) in the 2008–2011period. SST and fCO_{2w} show negative anomalies (Figure 8) in the

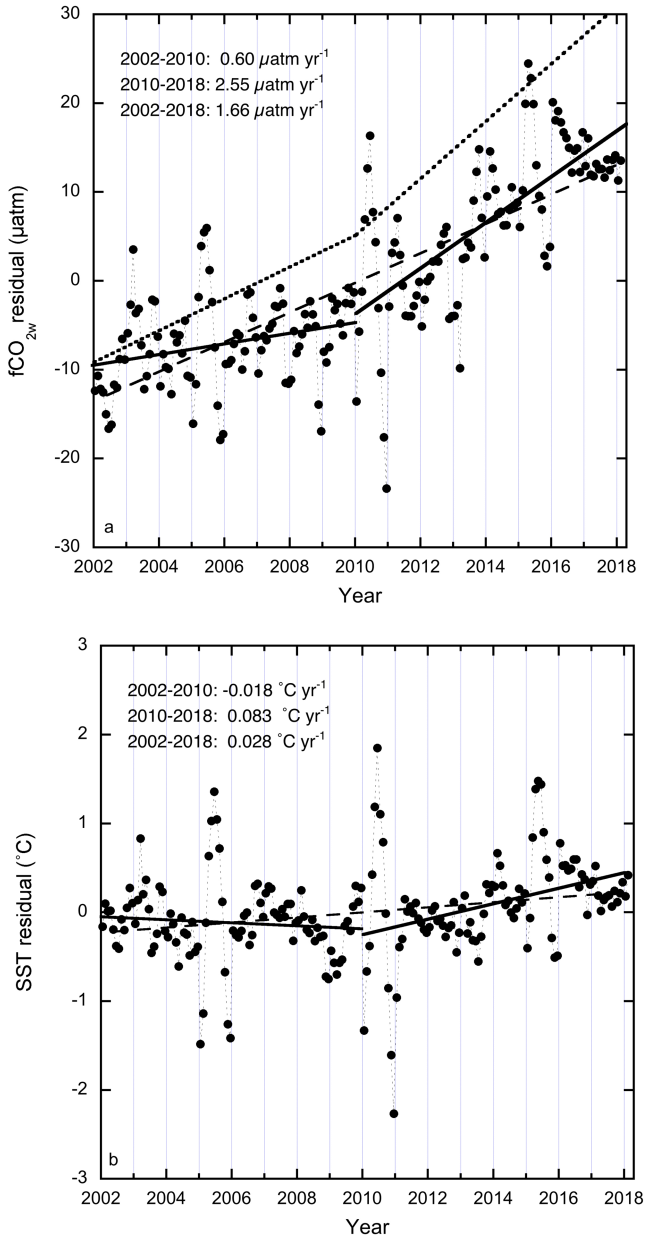


Figure 8. (a) Monthly residuals of fCO_{2w} (mapped product) from a harmonic fit, and trend lines of the residuals for 2002 to 2018 (long dashed line), for 2002 to 2010 (solid line), and from 2010 to 2018 (solid line). The short-dashed line is the expected trend if the fCO_{2w} followed atmospheric CO_2 increase and observed temperature trends as shown in panel b. From March 2002 to Feb 2010, the fCO_{2w} trend is 0.60 μatm/year and from March 2010 onward it is 2.55 μatm/year; b. SST (gridded OISST product) with trends from 2002 to 2010 of −0.02 °C/year and from 2010 to 2018 of 0.083 °C/year.

fall/winter of 2010 and in 2011. A strong positive anomaly in SST and fCO_{2w} occurs in the summer of 2010. These anomalies have a determining impact the multi-year trends.

The trends can be put in context of the rising atmospheric CO_2 levels. At steady state, the fCO_{2w} would keep up with the atmospheric CO_2 rise of, on average, 2.21 ppm/year from 2002 to 2018 based on the data from the KEY and RPB stations. This rise in mole fraction of CO_2 in the marine boundary layer, XCO_{2a} translates to 2.13 μatm/year at 100% humidity and 27 °C for fCO_{2w}. Thus, for the first part of the record, the fCO_{2w} shows an appreciable lag while in the second part of the record the increase is greater than expected from invasion of CO_2 from the atmosphere. Over the entire 16 years, the fCO_{2w} has increased but it is appreciably less than expected if the Caribbean Sea had kept up with the atmospheric increase leading to a deficit of 13 μatm (24%) compared to the expected trend by the end of the record. The short-dashed line in Figure 8a is the expected trend in the residual if the fCO_{2w} followed atmospheric CO_2 increase and SST trends (Figure 8b).

4.4. Attribution of Trends in fCO_{2w}

For the attribution of multiyear trends, we first describe the statistical correlations between the variables in the gridded mapped product. This is followed by the description of how SST and MLD impact the trends. Finally, the effect of temperature, gas exchange, biology, and mixing (B&M) on multiyear trends fCO_{2w} are described. No single overriding cause for the large change in trend in fCO_{2w} is apparent but rather it is a combination of factors, including multiyear seasonal anomalies in the middle part of the record that cause the large changes in fCO_{2w} trends.

The correlation analysis of the gridded data provides a summary of the correlation of fCO_{2w} with the environmental parameters as well as correlations between the different parameters (Figure 9). For the whole mapped product, the strongest dependency of fCO_{2w} is with temperature (positive) but there are also statistically significant correlations (at >90% confidence level) with wind (negative), position (negative), MLD (negative), and NFLH (positive). The fCO_{2w} shows insignificant statistical dependency on SSS. The sign of the correlations indicates that fCO_{2w} increases in response to the SST increase and decrease in response to increasing wind. The fCO_{2w} is negatively related with mixed layer depth indicating that deeper mixed layers lead to lower fCO_{2w}. The NFLH shows a positive correlation with fCO_{2w}, similar to what was shown in the sub-annual analysis, contrary to the expectation that greater fluorescence would indicate higher productivity and thus lower fCO_{2w}. The unexpected signs of the correlations of fCO_{2w} with MLD and NFLH are, in part, due to parameters being cross-correlated such that the statistical relations do not always imply causality. For example, SST and MLD are negatively correlated and the strong dependency of fCO_{2w} on SST will decrease the effect of entrainment of DIC due to mixed layer deepening. The NFLH and mixed layer depth are positively correlated, while fCO_{2w} and MLD are negatively correlated confounding simple causal relationships of the fCO_{2w} with individual parameters. The positive sign and weak correlations suggest that NFLH is not a strong predictor of the effect of productivity on fCO_{2w} in the region.

For the whole time period from 2002 to 2018, there is no statistically significant trend in observed SST but there is a decreasing trend in the observed SST from March 2002 to February 2010 of −0.178 ± 0.002 °C/year (P value < 0.001) and increasing from March 2010 to February 2018 of 0.194 ± 0.001 °C/year (P value = 0;

Table 2
The 3-Year Trends in fCO_{2w} (µatm/year) Versus Time[a]

Start/End	2002	2005	2008	2010	2011	2014	2017	2018
2002		0.7	−1.3	−1.8	−1.5	−0.6	1.1	1.3
2005			−4.1	−4.0	−2.1	−0.3	1.9	2.0
2008				−5.9	1.1	2.6	4.1	4.0
2010						2.3	4.2	3.9
2011						3.5	4.3	3.9
2014							2.2	1.5
2017								
2018								

[a]The trends are determined from the gridded mapped product and color coded from strongly negative (dark green) to strongly positive (red). For example, from 2011 to 2017 the trend is strongly positive (red) at 4.3 µatm/year.

Figure 2). For the OISST 1° × 1° × mo mapped product for the whole region, the trends are smaller but of the same sign, −0.06 ± 0.05 °C/year from March 2002 to February 2010 and 0.075 ± 0.07 °C/year for March 2010 to February 2018. The lower trend is attributed to the inherent smoothing of the OISST and compensating differences in the region on a monthly basis compared to along the cruise tracks.

Of the parameters investigated, SST has the greatest influence on fCO_{2w}. Based on the relationship of $\partial fCO_{2w}\,(\partial SST)^{-1}$ of 0.042 $°C^{-1}$, which under average conditions in the Caribbean Sea causes fCO_{2w} to change by ≈16 µatm per °C, the trend in observed fCO_{2w} due to surface ocean cooling/warming would be −2.9 µatm/year from 2002 to 2010 and 3.1 µatm year from 2010 to 2018 for the observed SST, and −1.0 and 1.2 µatm/year, using the mapped OISST product. Figure 8a includes trend lines depicting the changes in fCO_{2w} expected due to changes in atmospheric CO_2 and SST (thermodynamic effect) for the OISST mapped product in these periods.

The fCO_{2w} trends are affected by seasonal changes in MLD as shown in Park and Wanninkhof (2012). They showed that the wintertime fCO_{2w} decreased in the northeastern part of the study region from 2002 to 2009. This was attributed to longer periods with deep mixed layer depth (>30 m) providing more volume for CO_2 uptake and thus small changes in fCO_{2w} due to gas exchange. The summertime fCO_{2w} increased over the same time period. However, on annual scale the fCO_{2w} remained invariant thereby increasing the uptake significantly. Following this study, a more detailed investigation of the seasonal controls on fCO_{2w} trends

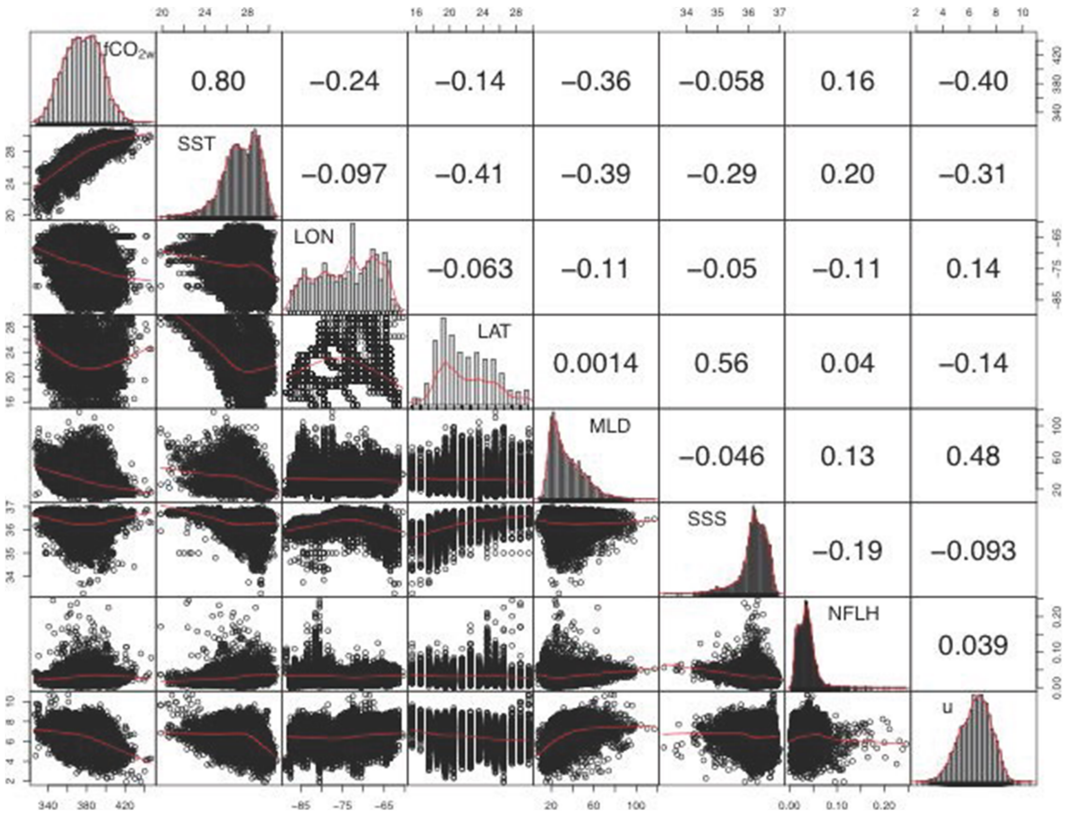


Figure 9. Correlogram of fCO_{2w}, SST, Lon, Lat, MLD_{Hycom}, SSS, NFLH (remotely sensed), and <*u*>, (remotely sensed) for the 1° × 1° × mo gridded data along the cruise lines from 2002 to 2018. Histograms of the relevant parameters are provided in the diagonal boxes from top left to bottom right. Below the diagonal are the scatter plots of the parameters. Above the diagonal are the correlation coefficients (*r*). For example, the histogram in the first row and first column is the fCO_{2w} distribution; the scatter plot on second row and first column shows the plot of fCO_{2w} versus SST; the first row and second column give the correlation between SST and fCO_{2w} of 0.8.

Table 3
Trends in SST, MLD, and fCO_{2w} for Wintertime and Summertime[a]

Range	Data	SST	SST	MLD	MLD	fCO_{2w}	fCO_{2w}
		Min/Winter	Max/Summer	Min/Summer	Max/Winter	Min/Winter	Max/Summer
2002–2018	Mapped product	0.05 ± 0.02	0.03 ± 0.01	0.27 ± 0.09	0.23 ± 0.14	1.72 ± 0.18	1.65 ± 0.17
	Gridded data	0.02 ± 0.05	−0.02 ± 0.03			1.39 ± 0.64	1.44 ± 0.33
	Mapped@Obs	0.04 ± 0.04	0.00 ± 0.03	0.28 ± 0.14	0.36 ± 0.23		
2002–2010	Mapped product	−0.01 ± 0.04	0.05 ± 0.03	−0.27 ± 0.12	0.06 ± 0.37	−0.06 ± 0.32	1.37 ± 0.5
	Gridded data	−016 ± 0.10	−0.02 ± 0.05			−2.64 ± 1.01	1.12 ± 0.65
	Mapped@Obs	−0.14 ± 0.08	−0.01 ± 0.05	−0.33 ± 0.14	0.99 ± 0.64		
2010–2018	Mapped product	0.12 ± 0.04	0.02 ± 0.05	0.78 ± 0.24	0.55 ± 0.34	2.82 ± 0.46	2.10 ± 0.48
	Gridded data	0.26 ± 0.07	0.16 ± 0.08			4.67 ± 0.95	3.33 ± 0.74
	Mapped@Obs	0.24 ± 0.06	0.13 ± 0.07	1.06 ± 0.37	0.22 ± 0.47		

Note. Winter: December–February; Summer: June–August. Mapped product: the trends of the mapped fCO_{2w} on a 1° × 1° × mo grid. Gridded data: the trends from the gridded data, on a 1° × 1° × mo grid. Model@Obs: The trends from the models (MLD) or remotely sensed (OISST) for the pixels that have gridded data, 1° × 1° × mo.
[a]Values are per year (SST: °C/year, MLD: m/year, fCO_{2w}: μatm/year)

is performed here. The mapped monthly fCO_{2w}, MLD, and SST products are averaged into wintertime (December–February) and summertime (June–August) values. As with the annual analysis, there is a change in the midpart of the record in winter and summer patterns around 2010. The winter and summer trends for the 2002 to 2010 and 2010 to 2018 time frames are shown in Table 3.

The wintertime and summertime data are also investigated to determine differences in trends between gridded data products and mapped products for SST and MLD. For the 1° × 1° gridded data, the trends in in situ measured SST are compared with the OISST, denoted in Table 3 as Obs and Mapped@Obs, respectively. This indicates if there are biases in seasonal trends using the MLRs to estimate fCO_{2w}, compared to measured fCO_{2w}.

Over the entire period 2002–2018, the trends during summer and winter for the mapped product and gridded data are consistent but with some differences (Table 3). Wintertime SST shows a slight warming for the mapped product and gridded data of ≈0.02 to 0.05 °C/year. The summertime OISST for the whole region show an increase as well of 0.03 ± 0.01 °C/year while observations along the cruise tracks are showing a non-significant cooling with a change of −0.02 ± 0.03 °C/year. The OISST at the sampling locations show no trend but overall the observations, gridded data, and mapped products agree to within their uncertainties. The MLD shows an appreciable increase of ≈0.3 m/year over the 16-year time period with general correspondence between summer and winter.

When breaking down the summer/winter trends into two time periods, differences are more apparent between the gridded data and the gridded mapped products. From 2002 to 2010, the gridded SST data along the cruise tracks show a decrease of ≈−0.16 °C/year in wintertime and no significant change in summer. The whole region, however, does not show a strong trend in OISST in winter. The differences are in the western region, which was not well sampled by the ships during this time period. The area shows a slight warming in the OISST product. The MLDs show a decrease of 0.3 m/year in summer and a large increase of 1 m/year in wintertime at the observation. Summertime shallowing is the same but there is no deepening in the mapped product. This wintertime MLD increase at the observational grid points correlates with the SST decrease during this period and similarly the lack of SST and MLD change in the mapped product. As a result, the fCO_{2w} shows a decrease of −0.06 (regional mapped product) to −2.64 (mapped) μatm/year during the wintertime and an increase of 1.37 (mapped) to 1.12 μatm/year (gridded) in the summer. Thus, during 2002–2010, the steady (mapped) or decreasing fCO_{2w} (gridded) are largely driven by the trends in wintertime similar to the results for one location as presented in Park and Wanninkhof (2012).

For the 2010–2018 time period, there are coherent positive trends for both winter and summer with SST increasing 0.2 °C/year. The MLD increases, particularly strongly in the summertime, and the fCO_{2w} increases on the order of 2 to 4 μatm/year. Winter and summertime trends for fCO_{2w} are also more similar compared to the 2002–2010 time frame where the seasonal trends diverged. The increases in fCO_{2w} and SST are significantly higher for the gridded data than for the mapped product for the whole region, again indicating that the trends in fCO_{2w} and forcing functions are stronger in the areas along the cruises' tracks.

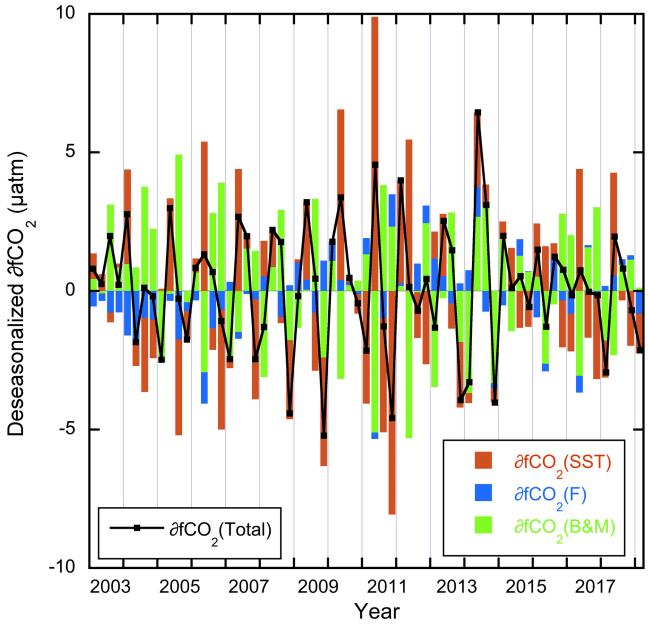


Figure 10. The deseasonalized δfCO_{2w} (SST; red bar); δfCO_{2w} (Bio&Mix; green bar); δfCO_{2w} (F_{CO2}; blue bar); and δfCO_{2w}(Total) (black squares connected with black line) plotted for 3-month intervals from 2002 to 2018.

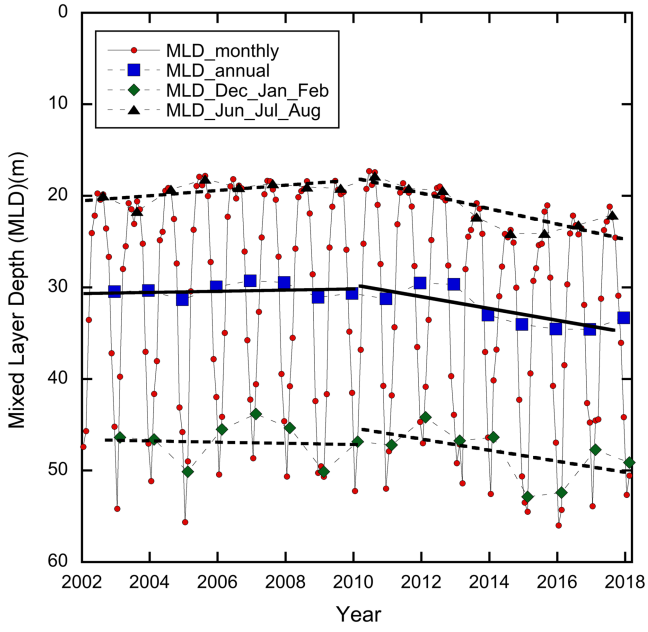


Figure 11. The monthly mixed layer depths (MLD) from the HYCOM model for the region from 2002 to 2018 (thin black line solid red circles). The annual means are shown as blue squares. The average MLD from June to August for each year are the green triangles, and the MLD from December to February are shown as green diamonds. The solid black lines show the trend annual means from 2002 to 2010 and 2010 to 2018. The dashed lines show the trend in summertime minimum and wintertime maximum mixed layer.

To further elucidate the physical and biogeochemical factors contributing to the observed trends in fCO_{2w} over the entire period, the same deconvolution is used as for the seasonal attribution (equation (8)). The monthly values of δfCO_{2w}(SST), $\delta fCO_{2w}(F_{CO2})$, and δfCO_{2w}(B&M) are determined from 2002 to 2018. Then the16-year average monthly values (Figure 7) are subtracted to deseasonalize the δfCO_{2w} data in order to determine the monthly anomalies over the 16-year record. To discern seasonal anomalous patterns, 3-month averages are used (Figure 10). The deseasonalized record shows a general anticorrelation of δfCO_{2w}(SST) and δfCO_{2w}(B&M) for the times with large deviations. This suggests that during anomalous warming, there is increased biological drawdown, and during cooling higher fCO_{2w} likely caused by mixing. However, for small δfCO_{2w}, the δfCO_{2w}(SST), and the δfCO_{2w}(B&M) can act synergistically or antagonistically.

The $\delta fCO_{2w}(F_{CO2})$ shows smaller seasonal anomalies compared to δfCO_{2w}(SST) and δfCO_{2w}(B&M). However, the δfCO_{2w} (F_{CO2}) shows persistent trends and is negative at the start of the record from 2002 to 2007, that is, air-sea gas flux causes a net loss of carbon in the mixed layer. It is predominantly positive from 2008 up to 2013. It does not show strong positive or negative values from 2013 onward.

Figure 10 shows large positive and negative excursions of seasonal δfCO_{2w}(SST) and δfCO_{2w}(B&M) in the middle of the record, from 2009 to 2011. The large changes in deseasonalized δfCO_{2w}(SST) are opposed by δfCO_{2w}(B&M). From 2009 to 2010, the springtime positive δfCO_{2w}(SST) is compensated by a negative late fall/wintertime δfCO_{2w}(SST). The δfCO_{2w}(B&M) shows an opposite phase to the large excursions in δfCO_{2w}(SST), but they are smaller magnitude to δfCO_{2w}(SST).

The change in trend in fCO_{2w} in the middle part of the record (2009–2011) is strongly influenced by anomalous physical and associated biogeochemical conditions in this time period. In the 2009–2011 transition, there are 3 consecutive years of large positive changes in δfCO_{2w}(SST) in Spring/Summer (Figure 10) and large negative δfCO_{2w}(SST) in fall/winter for 2010 and 2011. These changes are partially offset by opposing δfCO_{2w}(B&M). The net effect is that the processes lead to low fCO_{2w} from 2009 to 2011. This fCO_{2w} minimum has a large influence on the multiyear trends before and after. The period from 2010 to 2018 shows significantly smaller seasonal anomalies in the processes controlling fCO_{2w} as indicated by the smaller δfCO_{2w}(SST) and ∂pCO_{2w}(B&M) values.

Changes in MLD are an important contributor to the changes in δfCO_{2w} through its effect on SST, F_{CO2}, and B&M. The MLD influences ∂fCO_{2w}(SST) through cooling during MLD deepening and accelerated warming during shallowing. The $\partial fCO_{2w}(F_{CO2})$ is impacted by MLD as deeper mixed layers cause smaller changes in fCO_{2w} due to the volume effect. The MLD deepening impacts ∂fCO_{2w} (B&M) through differing and opposing means. Increased nutrient supply can enhance productivity that lowers fCO_{2w}, but increased DIC supply will increase fCO_{2w}. As shown in Figure 11, during the first part of the record from 2002 to 2010, the winters of 2004/2005 and 2008/2009 show mixed layers than are 5-m deeper than average. From 2010 to 2018, there is a general trend of increasing wintertime MLD with large increases (≈6 m) for the winters of 2015 and 2016 (Figure 11). The MLD increases appear a major contributor to the increase in trend of fCO_{2w} for the 2010–2018 time period.

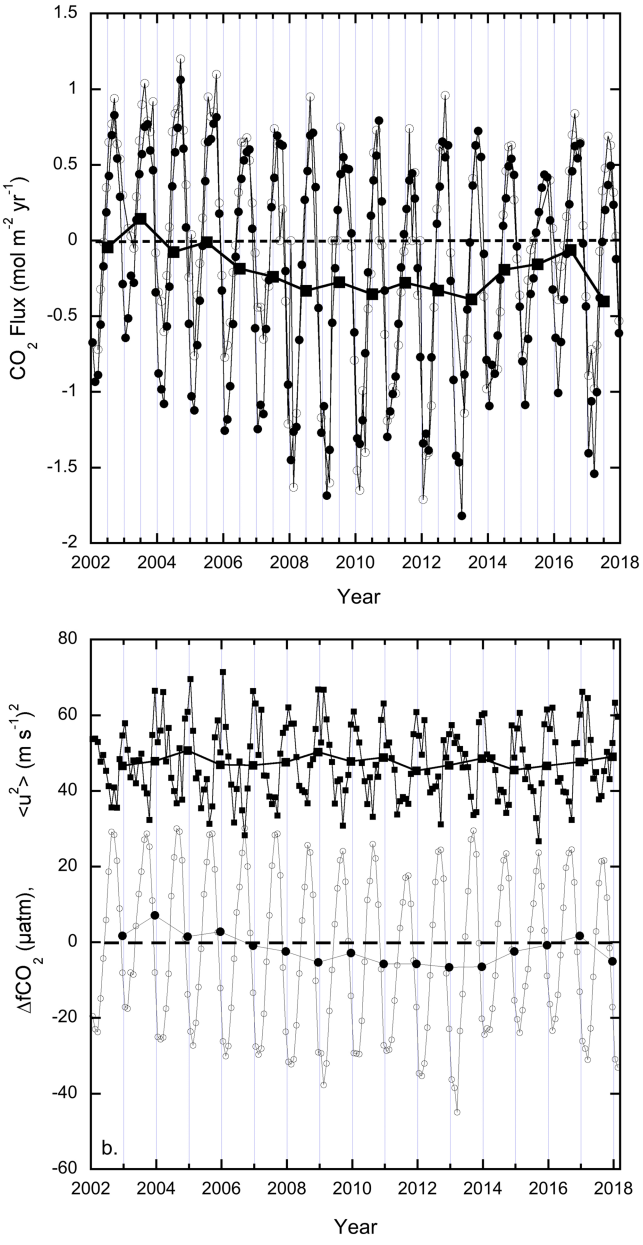


Figure 12. (a) Monthly air-sea CO_2 fluxes. The small solid squares are the fluxes determined from the mapped fCO_{2w} for the whole region using annual MLRs. The open circles are the gridded data along the track. The solid thick line and large squares are the annual averages for the whole region. (b) monthly ΔfCO_2 (open circles); annual ΔfCO_2 (solid circles, thick line); and monthly $<u^2>$ (black squares); annual $<u^2>$ (solid squares and thick line) for the mapped product for the whole region.

4.5. Air-Sea CO_2 Fluxes in the Caribbean

The air-sea CO_2 fluxes in the region are quantified by using the fCO_{2w} mapped product ($fCO_{2w,mapped}$). It is merged with the monthly averaged fCO_{2a} determined from the MBL product to determine the monthly ΔfCO_2. The OISST, SSS_{hycom}, and the second moment of the winds, $<u^2>$ are used to determine the monthly fluxes according to equations (5) and (6).

Overall, the seasonal progression in fCO_{2w} controls an air-sea CO_2 flux pattern that is characteristic for the subtropical and tropical regions of CO_2 outgassing in the summer and invasion in the winter (Bates et al., 2014; Takahashi et al., 2002). The monthly averaged CO_2 flux, $<u^2>$, and ΔfCO_2 over the 16-year period are shown in Figure 12 along with the annual means for the region. Winds show maxima in wintertime that are 50% greater than summertime values. The long-term trends in fluxes are in accord with the trends in ΔfCO_2, and changes in wind play a secondary role. There is no trend in $<u^2>$ from 2002 to 2018, but there are some multiannual anomalies. Of note is the increase in $<u^2>$ of 1.3% $year^{-1}$ during the wintertime from 2002 to 2010 and the weak increase in $<u^2>$ of 0.2% $year^{-1}$ in summertime from 2010 to 2018. For the wintertime from 2002 to 2010, the trend in flux is -0.08 (mol m^{-2} $year^{-1}$)$year^{-1}$ of which -0.01 (mol m^{-2} $year^{-1}$)$year^{-1}$ or 17% can be attributed to changes wind speed. For the weak positive trend in summertime fluxes from 2010 to 2018, the wind speeds contributed about the same (18%) despite the weaker trend $<u^2>$ as the absolute trend of efflux was smaller.

The multiannual trends in fluxes follow the same pattern as ΔfCO_2 with an increasing uptake from 2002 to 2010 and a decrease in uptake from 2010 to 2016. There is a reversal to an increase in uptake over the last year of the record (2017). For the whole region the average flux (uptake) is -11.1 ± 8.8 Tg/year from 2002 to 2018 where the uncertainty is the sd of the annual values. The average annual specific fluxes range from of 0.14 mol m^{-2} $year^{-1}$ in 2003, the only year of net outgassing, to -0.40 mol m^{-2} $year^{-1}$ in 2017 (Figure 12a). The total annual fluxes range from a net release of 8.0 Tg C $year^{-1}$ in 2003 to a strong uptake -22.4 Tg C $year^{-1}$ in 2017. The differences are primarily caused by differences in uptake during the winter months. In summertime, the region is a CO_2 source and shows less year-to-year variability than wintertime.

Annual anomalies of note are the maxima in uptake in 2013 and 2017 that are caused predominantly by large wintertime uptake. In 2017, there also is reduced summertime evasion (Figure 12a). While high wintertime uptake for 2013 and 2017 are mostly caused by the lower ΔfCO_2, in 2017 higher than average winter time winds contribute to the larger uptake as well. In addition to the effect high wintertime winds on the flux in 2017, low winds in the summer of 2015 significantly decreased the CO_2 evasion (Figures 12a and 12b).

The large changes in annual fluxes over preclude a clear indication that the CO_2 exchange in this marginal sea is appreciably different than the surrounding oceans as suggested in the ocean-dominated margin hypotheses of Dai et al. (2013). The hypothesis is that in waters the Caribbean Sea exchange with the open ocean through the passages and the subsequent vertical mixing causes slightly elevated fCO_{2w} and effluxes compared to the Atlantic Ocean basin. This was, in part-based interpretation of the results of Olsen et al. (2004), where Dai et al. (2013) suggest that fCO_{2w} are about 5 μatm higher in the Caribbean Sea than in the open ocean. As shown in Figure 12, 2003 had higher ΔfCO_2 and fluxes than seen in the following

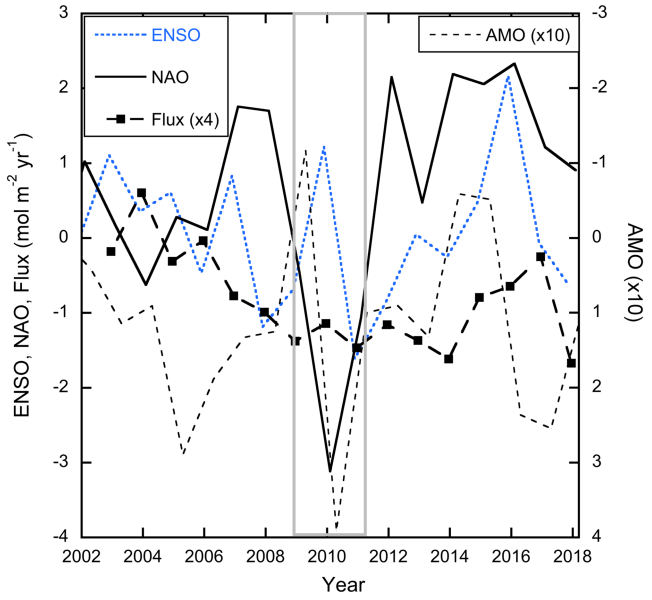


Figure 13. Annual air-sea CO_2 fluxes (black squares, thick dashed line) and climate indices: ENSO (blue short dashed line), NAO (solid line), and AMO (dashed line) plotted versus time. The indices are plotted for their peak season (see text). The AMO index is multiplied by 10 and its scale reversed (right axis). The annual fluxes that are multiplied by four on the left scale are plotted for year's end. For instance, the flux plotted at 2014 is for January to December 2013.

14 years. The Takahashi climatology (Takahashi et al., 2002) shows that on average the 14°N to 18°N latitude band in the open ocean is a weak source while the 18°N–26°N band is a net sink. These meridional trends and values are similar to observed in the region of the current study Caribbean Sea.

The means of determining the total CO_2 flux over the area has an impact on the results. All global and regional air-sea CO_2 flux estimates rely on interpolation of sparse data such that the large Caribbean dataset, and gridded data product can be used to provide a view of the differences. To estimate the effect of different temperatures, the average difference between the OISST product and measured temperatures on the ship of 0.25 °C is added the OISST and the mapped fCO_{2w} was determined with the MLRs in Table 1. This leads to mapped fCO_{2w} values that are on average 2 μatm higher and the average specific uptake decreases by 25% from −0.20 to −0.15 mol m^{-2} $year^{-1}$. This illustrates that accurate temperature measurements and means to interpolate the fCO_{2w} and SST from the intake depth to the water surface are important (Woolf et al., 2016).

The fluxes determined using gridded ΔfCO_2 data, and the mapped ΔfCO_2 based on the MLRs yield differences as well. The former only covers part of the region and has temporal gaps. Qualitatively, the two products agree. Both show similar large seasonal variations with the gridded data showing slightly greater amplitudes (Figure 12a). However, the average fluxes for the entire period differ greatly. They are -0.19 ± 0.70 mol m^{-2} $year^{-1}$ for the MLR based mapped product and -0.05 ± 0.70 mol m^{-2} $year^{-1}$ for estimate based on the gridded data. The differences in magnitudes of fluxes are attributed to lack of observations in the winter months, along with the use of observed SST in the gridded observations and OISST in the gridded mapped product. The OISST yields more negative fluxes as described above.

4.6. Relationship With Climate Reorganizations

The changes in fCO_{2w} and CO_2 fluxes on seasonal to interannual timescales are closely related to SST and MLD. In turn, the regional scale SST anomalies are associated with changes in the physical environment influenced by large-scale climate reorganizations. The climate cycles in the Caribbean are linked, through teleconnections, to the El Niño–Southern Oscillation, ENSO; the Atlantic Multidecadal Oscillation, AMO; and North Atlantic Oscillation, NAO (Birkmark, 2014; Ibánhez et al., 2017; Lefèvre et al., 2013, 2014; Thomas et al., 2008). Since the meteorological and oceanic responses to the climate indices are complex and sometimes lagged, only a broad view of responses of air-sea CO_2 fluxes to these climate patterns are investigated using the seasonal indices that have the greatest impact, for the NAO this is the wintertime (December–February), for the AMO spring (March–May), and for the ENSO the early winter (November–January).

Time series of these seasonal climate indices and annual CO_2 fluxes are shown in Figure 13, each showing significant anomalies in the middle part of the record (2009–2011) where the change in flux trends occurred. The annual fluxes in Figure 14 are plotted at year's end to reflect the expected lag between the indices and the annual cumulated flux. The overall trend in the NAO is positive for the time period, much like the preceding two decades (Thomas et al., 2008), but it shows a large minimum in 2010 that corresponds to the minimum in CO_2 flux (maximum uptake). The AMO shows a large negative followed by a positive excursion in 2009/2010 similar to the reversals in SST and fCO_{2w} anomalies, and the ∂pCO_{2w} (SST) (Figure 11) observed during this time. These changes in annual fluxes in response to the AMO are opposite to the changes observed in the Equatorial Atlantic (Ibánhez et al., 2017). The air-sea CO_2 fluxes show a positive relationship with ENSO with greater uptake during the negative phase of the ENSO (El Niño conditions). This is synergistic with the decreased evasion in the Equatorial Pacific albeit fivefold less in magnitude compared to the El Niño induced depressed outgassing in the Equatorial Pacific

upwelling region (Feely et al., 2006). The mechanisms for the lower fluxes in the Equatorial Pacific and Caribbean differ as well. The increased uptake in the Caribbean in response El Niño is due to prevailing lower SSTs. In the Equatorial Pacific, the decrease fCO_{2w} is due to decreased upwelling of waters with high DIC. In contrast, the greater uptake in the Caribbean is antagonistic with the Western Equatorial Atlantic where outgassing is enhanced during El Niño phase of ENSO (Lefèvre et al., 2013). The last year of the record (2017) shows an increase in CO_2 uptake along with a decrease in the ENSO and NAO indices. Although the magnitudes of the indices are not extreme, the change from 2016 to 2017 are large for the NAO and AMO. The increasing MLD and $<u^2>$, and decreasing SST in response to the decreasing NAO and increasing AMO, leads to increased CO_2 uptake.

The correspondence of the fluxes with climate indices is apparent, in particular when considering year-to-year changes, in addition to absolute magnitude. The ENSO and NAO minima correspond to lower SST and deeper MLD contributing to lower fCO_{2w} and a minimum in flux, or greater uptake. The change from low trend in fCO_{2w} in 2010/2011 to a much greater rate of increase corresponds to extrema in all the climate indices. The winters of 2010 and 2011 showed anomalous low SSTs for much of the North Atlantic, including the Caribbean (Buchan et al., 2013). Rivière and Drouard (2015) point out the contrasting phase of the NAO during 2010 and 2014. The negative NAO index in 2010 corresponds to low SST and low fCO_{2w} while maximum in the NAO in 2014 is associated with higher SSTs and fCO_{2w}. This suggests that the 3- to 8-year trends are strongly influenced by large single-year anomalies in the climate indices.

The effect of the AMO in forcing of the fluxes is less apparent but the large swing in 2009/2010 corresponds to large changes in the trend of fCO_{2w}. Indeed, the midpart of the record show that all indices have large anomalies (Figure 13) corresponding with a minimum in fCO_{2w} and largest uptake. However, the multifacetted impacts and monthly variation of the indices along with the large seasonal cycle of fCO_{2w} precludes a simple statistical or strong causal relationship for the entire period.

5. Conclusions

Through a corporate, academic and federal partnership the Caribbean Sea has changed from an undersampled area for surface water CO_2 and air-sea CO_2 fluxes to one of the best-observed regions in the world. The high sampling density and robust interpolation methods utilizing the strong correlation of fCO_{2w} with SST and other variables make it possible to discern strong decadal trends for the whole area in spite of seasonal variability that is 10 times greater. The region shows an average net uptake of CO_2 of -11.1 Tg C year^{-1} for 2002–2018 with annual fluxes ranging from +8.2 (evasion) in 2003 to -22.4 Tg C year^{-1} in 2017 in contrast to the annual climatological values in the region of 0.4 Tg C year^{-1} (Takahashi et al., 2009). Our results show that the general view of net outgassing in low latitude seas needs to be reassessed. Moreover, decadal variability of regional air-sea fluxes in oligotrophic marginal seas should be accounted for. In this work, much lower than expected fCO_{2w} increases prevailed for 8 years with major transition in patterns and trends occurring around 2010, closely associated with changes in SST trends and MLD that have a direct impact and indirect effect, though biological processes, on fCO_{2w}. The fCO_{2w} minima corresponds to anomalous low wintertime SSTs and extrema in several major climate indices, most notably the NAO. The fCO_{2w} hardly changed from 2002 to 2010 and strongly increased from 2010 to 2018. Over the entire time period the surface ocean fCO_{2w} lagged the atmospheric CO_2 increase by 24% causing the uptake to increase over time. Annual fluxes show increasing uptake from 2002 to 2010 and a small decrease in uptake thereafter with a reversal in the last year full of the record (2017) to larger uptakes. The changes in flux are less dramatic that the fCO_{2w} trend from 2010 to 2018 as the XCO_{2a} and fCO_{2w} are both increasing such that the ΔfCO_2, and thus, the flux does not change as much as fCO_{2w}. The trends and pattern are similar for the observations and the interpolated products, but magnitudes vary indicating that quantitatively assessing changes in fCO_{2w} and air-sea CO_2 fluxes requires both high density and quality data without temporal gaps, and robust approaches for spatial and temporal interpolation.

Acknowledgments
This work would not have been possible without support from Royal Caribbean Cruise Lines who have provided access to their ships and significant financial, personnel, and infrastructure resources for the measurement campaign coordinated through the Rosenstiel School of Marine and Atmospheric Sciences of the University of Miami. In addition to pCO_2 measurements, skin temperature (MAERI), TSG, optics, and ADCP operations take place on the ships. Peter Ortner and Elizabeth Williams of Rosenstiel School of Marine and Atmospheric Sciences have been instrumental keeping the science efforts going. Denis Pierrot, Kevin Sullivan, Robert Castle (ret.), and Betty Huss of NOAA AOML have led the maintenance and data processing and posting of fCO_2 data. All original fCO_{2w} data and gridded and mapped data products can be found at: www.aoml.noaa.gov/ocd/gcc website. David Munro INSTAR, ESRL/GMD provided the KEY and RPB CO_2 data on March 2018. NOAA High Resolution SST data were provided by the NOAA/OAR/ESRL PSD through://www.esrl.noaa.gov/psd/). The NOAA office of Oceanic and Atmospheric Research is acknowledged for financial support, in particular the Global Ocean Monitoring and Observations (fund reference 100007298) and the NOAA/OAR Ocean Acidification Program. We appreciate the thorough review of an anonymous reviewer and their suggestions on improving the statistical treatments.

References

Atlas, R., Hoffman, R. N., Ardizzone, J., Leidner, S. M., Jusem, J. C., Smith, D. K., & Gombos, D. (2011). A cross-calibrated multiplatform ocean surface wind velocity product for meteorological and oceanographic applications. *Bulletin of the American Meteorological Society*, *92*, 157–174. https://doi.org/10.1175/2010BAMS2946.1

Bakker, D. C. E., Pfeil, B., Landa, C. S., Metzl, N., O'Brien, K. M., Olsen, A., et al. (2016). A multi-decade record of high-quality fCO_2 data in version 3 of the Surface Ocean CO_2 Atlas (SOCAT). *Earth System Science Data*, *8*, 383–413. https://doi.org/10.5194/essd-8-383-2016

Bates, N. R., Astor, Y. M., Church, M. J., Currie, K., Dore, J. E., González-Dávila, M., et al. (2014). A time-series view of changing ocean chemistry due to ocean uptake of anthropogenic CO_2 and ocean acidification. *Oceanography*, *27*, 126–141. https://doi.org/10.5670/oceanog.2014.16

Bates, N. R., Samuels, L., & Merlivat, L. (2001). Biogeochemical and physical factors influencing seawater fCO_2 and air-sea CO_2 exchange on the Bermuda coral reef. *Limnology and Oceanography*, *46*, 833–846.

Bender, M., Doney, S., Feely, R. A., Fung, I. Y., Gruber, N., Harrison, D. E., et al. (2002), A large scale carbon observing plan: In situ oceans and atmosphere (LSCOP) *Report*., 201 pp, Nat. Tech. Info. Services, Springfield.

Birgmark (2014), El Niño–Southern Oscillation and North Atlantic Oscillation induced sea surface temperature variability in the Caribbean Sea, 27 pp, University of Gothenburg, Gothenburg. https://gvc.gu.se/digitalAssets/1503/1503953_b830.pdf

Buchan, J., Hirschi, J. J. M., Blaker, A. T., & Sinha, B. (2013). North Atlantic SST anomalies and the cold North European weather events of winter 2009/10 and December 2010. *Monthly Weather Review*, *142*(2), 922–932. https://doi.org/10.1175/MWR-D-13-00104.1

Cai, W.-J., Hu, X., Huang, W.-J., Wang, Y., Peng, T.-H., & Zhang, X. (2010). Alkalinity distribution in the Western North Atlantic Ocean margins. *Journal of Geophysical Research Oceans*, *115*, C08014. https://doi.org/10.1029/2009JC005482

Dai, M., Cao, Z., Guo, X., Zhai, W., Liu, Z., Yin, Z., et al. (2013). Why are some marginal seas sources of atmospheric CO_2? *Geophysical Research Letters*, *40*, 2154–2158. https://doi.org/10.1002/grl.50390

de Boyer Montégut, C., Madec, G., Fischer, A. S., Lazar, A., & Iudicone, D. (2004). Mixed layer depth over the global ocean: An examination of profile data and a profile-based climatology. *Journal of Geophysical Research*, *109*, C12003. https://doi.org/10.1029/2004JC002378

Dlugokencky, E. J., K. W. Thoning, P. M. Lang, and P.P. Tans (2017), NOAA Greenhouse gas reference from atmospheric carbon dioxide dry air mole fractions from the NOAA ESRL carbon cycle cooperative global air sampling network. Data path: ftp://aftp.cmdl.noaa.gov/data/trace_gases/co2/flask/surface/.

Dore, J. E., Lukas, R., Sadler, D. W., Church, J., & Karl, D. (2009). Physical and biogeochemical modulation of ocean acidification in the central North Pacific. *Proceedings of the National Academy of Sciences of the United States of America*, *106*, 12,235–12,240.

Fawcett, S. E., Lomas, M. W., Ward, B. B., & Sigman, D. M. (2014). The counterintuitive effect of summer-to-fall mixed layer deepening on eukaryotic new production in the Sargasso Sea. *Global Biogeochemical Cycles*, *28*, 86–102. https://doi.org/10.1002/2013GB004579.

Fay, A. R., & McKinley, G. A. (2013). Global trends in surface ocean pCO_2 from in situ data. *Global Biogeochemical Cycles*, *27*, 541–557. https://doi.org/10.1002/gbc.20051.

Feely, R. A., Takahashi, T., Wanninkhof, R., McPhaden, M. J., Cosca, C. E., & Sutherland, S. C. (2006). Decadal variability of the air-sea CO_2 fluxes in the Equatorial Pacific Ocean. *Journal of Geophysical Research*, *111*, CO8S90. https://doi.org/10.1029/2005JC003129

Gledhill, D. K., Wanninkhof, R., Millero, F. J., & Eakin, M. (2008). Ocean acidification of the greater Caribbean region 1996-2006. *Journal of Geophysical Research*, *113*, C10031. https://doi.org/10.1029/2007JC004629

Gruber, N., Keeling, C. D., & Stocker, T. F. (1998). Carbon-13 constraints on the seasonal inorganic carbon budget at the BATS site in the northwestern Sargasso Sea. *Deep Sea Research Part I: Oceanographic Research Papers*, *45*(4), 673–717. https://doi.org/10.1016/S0967-0637(97)00098-8

Holte, J., Talley, L. D., Gilson, J., & Roemmich, D. (2017). An Argo mixed layer climatology and database. *Geophysical Research Letters*, *44*, 5618–5626. https://doi.org/10.1002/2017GL073426

Huang, P., & Imberger, J. (2010). Variation of pCO_2 in ocean surface water in response to the passage of a hurricane. *Journal of Geophysical Research*, *115*, C10024. https://doi.org/10.1029/2010JC006185

Ibánhez, J. S. P., Flores, M., & Lefèvre, N. (2017). Collapse of the tropical and subtropical North Atlantic CO_2 sink in boreal spring of 2010. *Scientific Reports*, *7*. https://doi.org/10.1038/srep41694.

Jackson, J. B. C., M. K. Donovan, K. L. Cramer, and V. V. Lam (Eds.) (2014), Status and Trends of Caribbean Coral Reefs: 1970-2012, Global Coral Reef Monitoring Network, IUCN, Gland, Switzerland.

Kleypas, J. A. (1999). Geochemical consequences of increased atmospheric carbon dioxide on coral reefs. *Science*, *284*, 118–120.

Lefèvre, N., Caniaux, G., Janicot, S., & Gueye, A. K. (2013). Increased CO_2 outgassing in February–May 2010 in the tropical Atlantic following the 2009 Pacific El Niño. *Journal of Geophysical Research: Oceans*, *118*, 1645–1657. https://doi.org/10.1002/jgrc.20107

Lefèvre, N., & Taylor, A. (2002). Estimating pCO_2 from sea surface temperatures in the Atlantic gyres. *Deep-Sea Research Part I*, *1*(49), 539–554.

Lefèvre, N., Urbano, D. F., Gallois, F., & Diverrès, D. (2014). Impact of physical processes on the seasonal distribution of the fugacity of CO_2 in the western tropical Atlantic. *Journal of Geophysical Research: Oceans*, *119*, 646–663. https://doi.org/10.1002/2013JC009248

Lopez, R., Lopez, J. M., Morell, J., Corredor, J. E., & Del Castillo, C. E. (2013). Influence of the Orinoco River on the primary production of eastern Caribbean surface waters. *Journal of Geophysical Research: Oceans*, *118*, 4617–4632. https://doi.org/10.1002/jgrc.20342

Melendez Oyola, M., J. Salisbury, D. Gledhill, C. Langdon, J. Morell, D. Manzello, et al. (2018). Seasonal net ecosystem metabolism of the near-shore reef system in La Parguera, Puerto Rico, 1-50 pp.https://doi.org/10.5194/bg-2018-408

Metzl, N., Corbière, A., Reverdin, G., Lenton, A., Takahashi, T., Olsen, A., et al. (2010). Recent acceleration of the sea surface fCO_2 growth rate in the North Atlantic subpolar gyre (1993–2008) revealed by winter observations. *Global Biogeochemical Cycles*, *24*, GB4004. https://doi.org/10.1029/2009GB003658

Olsen, A., Triñanes, J., & Wanninkhof, R. (2004). Sea-air flux of CO_2 in the Caribbean Sea estimated using in situ and remote sensing data. *Remote Sensing of Environment*, *89*, 309–325.

Park, G.-H., & Wanninkhof, R. (2012). A large increase of the CO_2 sink in the western tropical North Atlantic from 2002 to 2009. *Journal of Geophysical Research*, *117*, C08029. https://doi.org/10.1029/2011JC007803

Pierrot, D., E. Lewis, and D. W. R. Wallace (2006). MS Excel program developed for CO2 system calculations, edited, Carbon Dioxide Information Analysis Center, Oak Ridge National Laboratory, U.S. Department of Energy, Oak Ridge, Tennessee. https://doi.org/10.3334/CDIAC/otg.CO2SYSXLSCDIAC105a.

Pierrot, D., Neil, C., Sullivan, K., Castle, R., Wanninkhof, R., Lueger, H., et al. (2009). Recommendations for autonomous underway pCO_2 measuring systems and data reduction routines. *Deep Sea Research, Part II*, *56*, 512–522.

Reynolds, R. W., Smith, T. M., Liu, C., Chelton, D. B., Casey, K. S., & Schlax, M. G. (2007). Daily high-resolution blended analyses for sea surface temperature. *Journal of Climate*, *20*, 5473–5496.

Rivière, G., & Drouard, M. (2015). Understanding the contrasting North Atlantic Oscillation anomalies of the winters of 2010 and 2014. *Geophysical Research Letters*, *42*, 6868–6875. https://doi.org/10.1002/2015GL065493

Robbins, L. L., Daly, K. L., Barbero, L., Wanninkhof, R., He, R., Zong, H., et al. (2018). Spatial and temporal variability of pCO_2, carbon fluxes, and saturation state on the West Florida Shelf. *Journal of Geophysical Research: Oceans*, *123*, 6174–6188. https://doi.org/10.1029/2018JC014195

Soloviev, A. V., & Schlüssel, P. (1996). Evolution of cool skin and direct air-sea gas transfer coefficient during daytime. *Boundary-Layer Meteorology*, *77*, 45–68.

Takahashi, T., Olafsson, J., Goddard, J. G., Chipman, D. W., & Sutherland, S. C. (1993). Seasonal variation of CO_2 and nutrients in the high-latitude surface oceans: A comparative study. *Global Biogeochemical Cycles*, *7*, 843–878. https://doi.org/10.1029/93GB02263

Takahashi, T., Sutherland, S. C., & Kozyr, A.. (2017). Global ocean surface water partial pressure of CO_2 database: Measurements performed during 1957–2016 (Version 2016). ORNL/CDIAC-160, NDP-088(V2015). (NCEI Accession 0160492). Version 3.3. NOAA National Centers for Environmental Information. Dataset. [accessed 5/16/2018]

Takahashi, T., Sutherland, S. C., Sweeney, C., Poisson, A., Metzl, N., Tilbrook, B., et al. (2002). Global sea-air CO_2 flux based on climatological surface ocean pCO_2, and seasonal biological and temperature effects. *Deep-Sea Research Part II*, *49*, 1601–1622.

Takahashi, T., Sutherland, S. C., Wanninkhof, R., Sweeney, C., Feely, R. A., Chipman, D. W., et al. (2009). Climatological mean and decadal change in surface ocean pCO_2, and net sea-air CO_2 flux over the global oceans. *Deep-Sea Research Part II*, 554–577. https://doi.org/10.1016/j.dsr2.2008.12.009

Thomas, H., Friederike Prowe, A. E., Lima, I. D., Doney, S. C., Wanninkhof, R., Greatbach, R. J., et al. (2008). Changes in the North Atlantic Oscillation influence CO_2 uptake in the North Atlantic over the past 2 decades. *Global Biogeochemical Cycles*, *22*, GB4027. https://doi.org/10.1029/2007GB003167

Turk, D., Zappa, C. J., Meinen, C. S., Christian, J. R., Ho, D. T., Dickson, A. G., & McGillis, W. R. (2010). Rain impacts on CO_2 exchange in the western equatorial Pacific Ocean. *Geophysical Research Letters*, *37*, L23610. https://doi.org/10.1029/2010GL045520

Wanninkhof, R. (2014). Relationship between wind speed and gas exchange over the ocean revisited. *Limnology and Oceanography: Methods*, *12*, 351–362. https://doi.org/10.4319/lom.2014.12.351

Wanninkhof, R., Olsen, A., & Triñanes, J. (2007). Air-sea CO_2 fluxes in the Caribbean Sea from 2002-2004. *Journal of Marine Systems*, *66*, 272–284.

Weiss, R. F. (1974). Carbon dioxide in water and seawater: the solubility of a non-ideal gas. *Marine Chemistry*, *2*, 203–215.

Weiss, R. F., & Price, B. A. (1980). Nitrous oxide solubility in water and seawater. *Marine Chemistry*, *8*, 347–359.

Woolf, D. K., Land, P. E., Shutler, J. D., Goddijn-Murphy, L. M., & Donlon, C. J. (2016). On the calculation of air-sea fluxes of CO_2 in the presence of temperature and salinity gradients. *Journal of Geophysical Research: Oceans*, *121*, 1229–1248. https://doi.org/10.1002/2015JC011427

Xue, Z., He, R., Fennel, K., Cai, W.-J., Lohrenz, S., Huang, W.-J., et al. (2016). Modeling pCO_2 variability in the Gulf of Mexico. *Biogeosciences*, *13*, 4359–4377. https://doi.org/10.5194/bg-13-4359-2016.

Yang, B., Byrne, R. H., & Wanninkhof, R. (2015). Subannual variability of total alkalinity distributions in the northeastern Gulf of Mexico. *Journal of Geophysical Research: Oceans*, *120*, 3805–3816. https://doi.org/10.1002/2015JC010780